SIMONE COLUCCI

MODELLING OF BUBBLE NUCLEATION IN TRACHY-PHONOLITIC MAGMAS: IMPLICATIONS FOR THE DYNAMICS OF ASH-RICH ERUPTIONS

MODELLING OF BUBBLE NUCLEATION IN TRACHY-PHONOLITIC MAGMAS: IMPLICATIONS FOR THE DYNAMICS OF ASH-RICH ERUPTIONS

SIMONE COLUCCI

PhD candidate in Earth Sciences, XXIV Course

Faculty of Mathematical, Physical and Natural Sciences
Earth Science

Supervisor:
Prof. Danilo M. Palladino
Cosupervisor:
Prof. Raffaello Trigila

September 2012

Simone Colucci: *Modelling of Bubble Nucleation in trachy-phonolitic magmas: implications for the dynamics of ash-rich eruptions,* PhD candidate in Earth Sciences, XXIV Course , September 2012

On fait la science avec des faits comme une maison avec des pierres; mais une accumulation de faits n'est pas plus une science qu'un tas de pierres n'est une maison. (H.J. Poincaré)

Science is made up of data as a house is made up of stones; but a heap of data is no more science than a pile of stones is a house

ABSTRACT

Nucleation of water gas bubbles in trachyphonolitic magmatic melts has been investigated integrating theory and numerical modelling with decompression experiments and analysis of natural ash samples of explosive eruptions. Bubble nucleation, considered the natural response of magmas to decompression, is strongly dictated by the gas-melt surface tension. Here, I use an integrated approach to quantify the role of the surface tension in the nucleation process combining high pressure - high temperature nucleation experiments with a numerical modelling based on the gradient theory (Cahn and Hilliard, 1959). This theory, successfully applied in several studies of industrial polymers (Poser and Sanchez, 1981; Harrison et al., 1999; Kahl and Enders, 2000; Enders et al., 2005) was never been used before to study systems of volcanological interest. I show that surface tension is far to be a constant, but it decreases with increasing nucleation pressure (i.e. the confining pressure). Entering the values of surface tension into the classical theory of nucleation, I obtain a variable supersaturation pressure triggering nucleation. The decreasing value of the gas-melt surface tension with increasing pressure, facilitate bubble nucleation at high pressure, thus enhancing the explosivity of eruptive events from deeper reservoirs. Instead, the hindered nucleation at relatively low pressure, due to high bubble surface tension, implies that the generation of explosive eruptions from shallow reservoirs requires high decompressions. Finally the vesiculation, in terms of nucleation and growth, of natural samples of ash-rich eruptions has been studied by applying a novel technique able to take 3D measurements of bubbles preserved on ash particle's surface. The Bubble Size Distributions (BSD), together with the field evidence, suggest that the ash production in these ash-rich eruptions, rather than to magma-water explosive interaction, is related to the high decompression necessary to nucleate bubbles in a shallow reservoir.

RIASSUNTO

E' stato investigato il processo di nucleazione di bolle di acqua allo stato gassoso in liquidi magmatici a composizione trachifonolitica integrando teoria e modellistica numerica con esperimenti di decompressione e analisi su ceneri vulcaniche prodotte da eruzioni a carattere esplosivo. Un approccio integrato, combinando esperimenti di nucleazione ad alta pressione-alta temperatura con un modello numerico basato sulla teoria del gradiente (Cahn and Hilliard, 1959), ha permesso di quantificare il ruolo della tensione superficiale nei processi di nucleazione. La teoria del gradiente, applicata con successo in numerosi studi di polimeri industriali (Poser and Sanchez, 1981; Harrison et al., 1999; Kahl and Enders, 2000; Enders et al., 2005) non era mai stata utilizzata precedentemente per problemi di interesse vulanologico. Nel presente lavoro di tesi viene mostrato che la tensione superficiale è tutt'altro che costante ma diminuisce all'aumentare

della pressione di nucleazione (i.e. pressione di confinamento). Inserendo i valori della tensione superficiale così ottenuti nella teoria classica della nucleazione, si ottiene che la pressione di sovrassaturazione per produrre nucleazione varia con la pressione di confinamento a cui si trova il sistema. La diminuzione della tensione superficiale gas-melt all'aumentare della pressione di confinamento facilita la nucleazione di bolle ad alta pressione, favorendo il carattere esplosivo degli eventi eruttivi associati a reservoir profondi. Invece, la difficoltà di nucleazione a pressione relativamente minore, dovuta all'elevata tensione superficiale, fa sì che la generazione di eruzioni esplosive da reservoir supericiali richieda elevati valori di decompressione. Infine è stata studiata la vescicolazione, in termini di nucleazione e crescita, su particelle di cenere prodotte da eruzioni ricche in cenere utilizzando una nuova metodologia in grado di effettuare misure 3D delle bolle conservate sulla superficie della particella di cenere. Le "Bubble Size Distribution" (BSD) dei campioni, congiuntamente alle evidenze di terreno, suggeriscono che il meccanismo di produzione della cenere per i casi esaminati, piuttosto che di tipo idromagmatico, sia da collegarsi all'elevata decompressione necessaria per nucleare bolle in serbatoi superficiali.

ACKNOWLEDGMENTS

I like to thank my academic advisors, Danilo Palladino, Raffaello Trigila and Maurizio Battaglia; the referees Alexander Proussevitch and Pierfrancesco Dellino for the helpful comments, Gopal Mulukutla for the technical support and the ideas, Mattia De Michieli Vitturi for their very helpful suggestions, Salomon Hailemikael for LaTeX assistance and tricks and Fabio Proietti for the images. I also wish to thank technical support provided by Nancy Cherim at the University of New Hampshire Instrumentation Center, by Marco Albano at the University of Rome 'Sapienza' and by Mauro Brilli at Istituto di Geologia Ambientale e Geoingegneria (IGAG)

CONTENTS

1

INTRODUCTION

Vesiculation process (i.e. bubble formation followed by growth) drives the magma rising into the conduit and triggers the explosive eruptions. Natural sample analysis (Cashman and Mangan, 1994; Mangan and Cashman, 1996; Mastrolorenzo et al., 2001; Polacci et al., 2001, 2003; Adams et al., 2006; Carey et al., 2009), laboratory experiments (Mangan and Sisson, 2000; Gardner et al., 1999; Hurwitz and Navon, 1994) and numerical modelling (Toramaru, 1989, 1990a,b) indicate that bubbles preserved on the volcanic particles represent a powerful tool to investigate magma storage conditions and intra-conduit dynamics, and correlate these with the eruptive style. This work is concerned with the initial stage of the formation of a gas phase: this process is called bubble nucleation. Bubble nucleation processes are often interpreted using the classical nucleation theory (Landau and Lifshitz, 1980). Nevertheless, the physics of nucleation may be more complex than the classical theory predicts. Therefore, as matter of application, the nucleation mechanism of gas bubbles of trachy-phonolitic compositions from the volcanic districts of Vulsini and Campi Flegrei (Central Italy) will be studied, combining data from natural products, laboratory experiments and numerical modelling. In particular the role of gas-melt surface tension, the main obstacle of bubble formation, will be explored. Finally the relation of the nucleation process with the eruptive style will be discussed, with implications on the intra-conduit vesiculation processes leading to fragmentation, to explain the ash formation in the ash-rich eruptions.

2

STATE OF THE ART AND MOTIVATIONS

Earth-scientists, in the last two decades, dedicated an increasing interest to gas bubble formation and growth (i.e. vesiculation) in magmas. Vesiculation triggers the eruption and drives the magma rising into the conduit. For this reason the study of vesiculation addresses the problem of eruptability of volcanic systems and of determining the eruptive style. From the physical point of view, nucleation and growth represent two independent processes working at different scales: nucleation is a molecular-scale phenomenon, growth is a macro-scale process. If the growth of gas bubbles can be described using the formulation of classical physics (Proussevitch et al., 1993), on the other hand processes related to nucleation have to be analysed from a different perspective, considering the dynamics of the molecules.

Up to now scientists used three different approaches to study vesiculation: the analytical examination of natural samples, analog or high-pressure high-temperature laboratory experiments, and numerical simulations. The following sections are mainly concerned with the initial stage of formation of a gas phase, nucleation. I will discuss the methods commonly used and the results obtained from the analysis of natural samples, from the laboratory experiments and numerical modelling. Finally I will explain the motivations of the present work.

2.1 THEORY AND NUMERICAL MODELLING OF BUBBLE NUCLEATION IN MAGMAS

The first systematic study of the physics of bubble nucleation in magmas was presented by Toramaru (Toramaru, 1989, 1990a,b). The author developed an analytical formulation for bubble nucleation combined with the growth rates and applied it to a numerical model to predict Bubble Size Distribution (BSD), imposing different initial conditions (e.g. depth, decompression rate, initial dissolved water concentration, etc.). In this model, nucleation is represented by the so called Classical Nucleation Theory (Landau and Lifshitz, 1980), a simple, widely used theory for the nucleation of a new fluid phase. Hurwitz and Navon (1994) and Navon and Lyakhovsky (1998) analysed the vesiculation processes in silicic magmas, discussing the modification to the classic formulation of the nucleation theory, in particular regarding the role of the so-called heterogeneous nucleation. To form a new phase, every system has to overcome a Free Energy barrier: this barrier strongly decreases when nucleation occurs on host sites (i.e. impurities in general) and in this case it is called heterogeneous, opposed to the classical homogeneous nucleation. Heterogeneous bubble nucleation is a function of the wetting angle (i.e. the angle between crystal and bubble), so it depends on the shape of the crystals. The role of heterogeneities in enhancing bubble nucleation is confirmed in experiments and it will be discussed in the next sections. The same authors (Hurwitz and Navon, 1994; Navon and Lyakhovsky, 1998) evi-

denced the fundamental role of supersaturation and surface tension, showing that nucleation rate is very sensitive to these two interplayed variables, but they did not quantify the value of surface tension along a magma-water interface. Also Proussevitch et al. (1993) evidenced the fundamental role of surface tension, discussing the critical radius of bubbles (i.e. the radius of the nuclear bubble). Blower et al. (2002) explored the evolution of BSD using a fractal model to describe the bubble distributions of observed samples. They formulated a model for a continuous fashion of nucleation events and subsequent growth to produce an increasing exponent of the 'power law' function, commonly observed in BSD of natural and experimental samples. This is in contrast with the interpretations of Gaonac'h et al. (1996) who attributed the same kind of distribution to coalescence rather than to multiple nucleation events. On the other hand, Proussevitch et al. (2007) highlighted that a power function cannot be formally a probability density but represents a truncation of a log logistic distribution for the large scale bubbles far beyond the distribution mode. This means that power law function, often used to characterize vesiculation of volcanic products, shifts the focus into the tail of the distribution that represents an inaccuracy because the distribution mode (i.e. the maximum of probability density function) represents the fundamental characterization of a statistical distribution. Finally Toramaru (2006) proposed a method, based on his previous model (Toramaru, 1989), to estimate decompression rate by using Bubble Number Density (number of bubbles per melt volume; BND) data of natural pumice samples from volcanic eruptions, highlighting a strong correlation between nucleation and explosive eruptive style.

2.2 EXPERIMENTAL STUDIES OF BUBBLE NUCLEATION IN MAGMAS

Experimental works (Mangan and Sisson, 2000; Gardner et al., 1999; Hurwitz and Navon, 1994) show that bubbles can nucleate during decompression on the surface of microlites in a crystal-bearing magma. Otherwise homogeneous bubble nucleation appears more difficult, basically because of the gas-melt surface tension. Low pressure (1 atm) and high temperature ($1200-1400^{\circ}C$) melting experiments by Bagdassarov and Dingwell (1993), using natural rhyolite obsidian with $0.1-0.2wt\%$ of water, show that crystals may serve as sites for heterogeneous bubble nucleation. A rhyolite containing $5-10\%$ in volume microlites vesiculates $10-100$ times faster than does crystal-free rhyolite. The same behaviour is also shown in the isothermal decompression experiments by Hurwitz and Navon (1994) and Gardner et al. (1999) using hydrous rhyolite saturated at $750-850^{\circ}C$ and $150-200MPa$. In their experiments, bubbles nucleate when the pressure is reduced 5 to 20 MPa below the initial saturation pressure. Mourtada Bonnefoi and Laporte (1999), using a uniform saturated rhyolite melt, show that pressure reductions of $150-200MPa$ may be required to trigger bubble nucleation in the absence of crystals. Also Mangan and Sisson (2000) find that in absence of microlites, nucleation does not occur until the supersaturation pressure reaches ca. $120MPa$.

In the last years, it has been recognized that surface tension profoundly influences the ability of gas bubbles to nucleate in silicate melts. Epelbaum

et al. (1973) obtain surface tensions of 0.061 and 0.072 J/m^2 for water-saturated rhyodacite at 950°C and 100 and 50MPa, respectively. Khitarov et al. (1979) obtain $0.090 - 0.170 J/m^2$ for basalt at 1200° and $100 - 500$MPa water pressure. Bagdassarov et al. (2000) provide more extensive data on hydrous synthetic haplogranite melt. Values of $0.065 - 0.135 J/m^2$ are obtained at $800 - 1200$°C and $100 - 400$MPa water pressure. They find a systematic increase with dissolved water and a less dramatic increase with increasing temperature. Mangan and Sisson (2005) evaluate surface tension in natural dacite melt water-saturated experimentally at 200MPa, $950 - 1055$°C and $5.7 - 4.8$*wt*% of water. Rather than traditional macroscopic measurements like Bagdassarov et al. (2000), the authors solve for surface tension the classical nucleation theory, finding value of about $0.01 - 0.03 J/m^2$ for water contents of $4 - 6$*wt*%. In order to further examine the impact of temperature on surface tension, Gardner and Ketcham (2011) and Gardner (2012) use the same method and find that surface tension increases with temperature, but only when temperature exceeds ca. 850°C. These last recent works calculate the surface tension solving the classical nucleation theory, hence assuming that this theory allows a successful description of the nucleation process and obtain results that are strictly dependent on nucleation.

2.3 NATURAL SAMPLE ANALYSIS

Textures of pyroclasts, specifically vesicle size distribution and vesicle shape, are quantified from image analysis and used to study intra-conduit processes (Cashman and Mangan, 1994; Mangan and Cashman, 1996; Mastrolorenzo et al., 2001; Polacci et al., 2001, 2003; Adams et al., 2006; Carey et al., 2009). The morphology of particles is used to distinguish the mechanism of fragmentation (i.e. magmatic vs hydromagmatic) through comparing the shape of natural samples with that ones obtained by experiments of magma-water interactions (Wohletz, 1983, 1986; Wohletz et al., 1995; Buttner and Zimanowky, 1997; Buttner et al., 1999, 2002, 2006; Austin Erickson et al., 2009). Hydromagmatic fragmentation has been invoked to explain the origin of ash in specific explosive eruptions (Dellino and La Volpe, 1996a; Dellino et al., 2001). Vesicle size distributions are a tool to constrain the relative timing of bubble nucleation, growth, coalescence, and potentially collapse in explosive eruptions and to understand how the chamber and conduit dynamics, driven by magma degassing, influence the eruptive behavior (Mangan et al., 1993; Cashman and Mangan, 1994; Polacci et al., 2001, 2003). In particular Carey et al. (2009) try to explain the origin of the ash-rich phase of the 1875 Askja eruption by relating the macroscopic evidence of transition of style with the microscopic evidence of the vesicles. Their conclusions are that the magma was a foam prior to fragmentation and that the ash-rich phases are not only related to a hydromagmatic fragmentation mechanism. However they do not solve the problem of the extensive ash production.

Scanning electron microscope, -SEM-, for highest magnification, and scanned images, for the lowest one, from polished thin sections are used to quantify textural features in pumices and scorias from individual stratigraphic levels (Adams et al., 2006; Carey et al., 2009) . The images, so obtained, are captured in grayscale and then processed. A manual editing of the images is yet required to

rebuild vesicle walls broken during thin section preparation. In addition, thin bubble walls are often erased during image acquisition or during the conversion from grayscale to binary and have to be redrawn. For each vesicle area measured, an equivalent diameter for a circle with the same area is calculated. Based on this diameter, vesicles are binned, and areal number densities are calculated for each bin . The binned data so obtained are plotted in a frequency histogram. Conversion from two-dimensional to three-dimensional number densities (i.e. number of vesicles within a certain size interval per unit volume), is performed using the method by Sahagian and Proussevitch (1998). The method relies on the intersection probabilities for spheres to convert each 2D bin-size. The stereology technique, conversion from 2D to 3D, is based on the idea that a random plane cutting a volume of objects with different sizes gives a 2D distribution that overstimates the ratio between large and smaller objects. The procedure to measure the bubbles and calculate the distribution received a great contribution by Polacci et al. (2006), Proussevitch et al. (2007), Polacci et al. (2010) and Proussevitch et al. (2011).

Proussevitch et al. (2007) propose an analytical and computational formulation to characterize bubble size ditribution (BSD) in a fully quantitative way. The authors show that all the known distributions belong to the logarithmic family of statistical distributions and propose a formulation to find the function that fits best the observed data. This approach allows to describe bubble data with a known probability distribution, using a standard procedure, overcoming the ambiguity related to the different visualization of the data. An important ouline of their paper is about the definition of the BND: it must be defined as number of bubbles per melt volume (not bulk volume, as traditionally used) because, the molar volume of dissolved volatiles is much smaller than that of bubbles/gases. Defining BND in this way, it remains invariant as bubbles grow and it is just a function of nucleation (assuming no coalescence). The details of the method will be discussed in the chapter 4.

Proussevitch et al. (2011) propose a new method to take 3D measurements using a Stereo SEM (SSEM), a scanning electron microscope with sample tilting capability. The technique is based on the imaging of vesicle fragments preserved on the ash-surface particles. The SSEM tilts the sample and measures images with different angles. The images so acquired are used to create a digital elevation model (DEM), a 'topography' of the particle. The method allows measurement of vesicles within a size range from one to over a million cubic microns.

2.4 MOTIVATIONS OF THE WORK

Nucleation of gas bubbles in magmas represents the main triggering of explosive eruptions. Classical nucleation theory predicts a very strong dependence of bubble nucleation rate on the supersaturation pressure and surface tension. While the role of supersaturation has been deeply explored in details (Mangan and Sisson, 2000; Gardner et al., 1999; Mourtada Bonnefoi and Laporte, 1999; Hurwitz and Navon, 1994; Bagdassarov and Dingwell, 1993), the role of surface tension is not still clear. Surface tension is usually calculated by decompression experiments in a crystal-free magma, solving for the surface tension the classical

theory of homogeneous nucleation. There is not guarantee that nucleation, in absence of crystals, occurs homogeneously. In other words, every kind of impurities in the melt could represent a host site for heterogeneous nucleation, making the assumption of homogeneous nucleation invalid. In the present work the surface tension will be calculated using a criterion independent from the nucleation theory. In particular the problem will be numerically solved using a statistical mechanics based model, where the surface tension is calculated using a model for a lattice fluid and considering interaction between molecules. The results are compared with nucleation experiments on a trachytic magma from Campi Flegrei (central Italy) to verify the effect of surface tension on nucleation processes. The experiments have been performed using a Mini Internal Heated Pressure Vessel, a novel experimental facility that allows a very fast pressure drop. Finally Bubble Size Distribution analysis (BSD) using Stereo-SEM technique has been applied on natural ash samples. Ash particles preserve information on the state of the magmatic foam, in terms of nucleation and growth, at the time it has undergone brittle fragmentation, so can give information on the mechanisms leading to ash formation. This kind of analysis has been applied to well-preserved ash-rich trachy-phonolitic eruptions, from the Quaternary Vulsini Volcanic District (central Italy), in which the fine-grained nature of deposits, even in near-vent settings, indicates negligible sorting by transport, implying the eruption of highly fragmented magmas.

3

CASE STUDIES

3.1 GROTTE DI CASTRO AND SOVANA ERUPTIONS

Two major explosive events of the Latera volcano, in the Vulsini Volcanic District (central Italy)(Fig.1), have been investigated in the present study, the Grotte di Castro and the Sovana eruptions (Vezzoli et al., 1987), for the occurrence of wide-dispersion ash-rich eruptive phases. Volcanism in the area occurred at five major volcanic complexes and spanned $0.6 - 0.1 Ma$ (Vezzoli et al., 1987; Palladino et al., 2010). Chemical compositions of the erupted products encompass a wide spectrum of potassic rock types with the major explosive eruptions trachytic to phonolitic in composition (Vezzoli et al., 1987; Palladino et al., 2010). The Latera Caldera is located in the western sector of the Vulsini Volcanic District and developed between $0.3 - 0.15 Ma$ from the polygenetic collapse of a stratovolcano.

The Latera activity was dominated by plinian and pyroclastic flow-forming eruptions leading to the emplacement of widespread pyroclastic fall and flow deposits around the present-day caldera and ended with strombolian, hydromagmatic and effusive activities from essentially monogenetic intra- and circumcaldera centers (Sparks, 1975; Vezzoli et al., 1987; Palladino and Valentine, 1995; Palladino and Agosta, 1997; Palladino et al., 2010).

3.1.1 *Grotte di Castro*

Based on the geochronological age determinations on the bracketing deposits, the Grotte di Castro eruption (hereafter GRC) has an inferred age of approximately 0.18 Ma (see Palladino et al., 2010 for an updated summary of available geochronological data). Here, I focus on the lower member of the Grotte di Castro eruptive succession (Fig. 2), which in relatively proximal settings includes early, decimeter-thick, strombolian (blackish scoria-bearing) and subplinian (whitish pumice-bearing) fallout horizons, followed by widespread meter-thick, ash-rich, dune-bedded, accretionary-lapilli-bearing surge deposits (Fig. 2).

The well-sorted strombolian scoria fall horizon has a maximum observed thickness of $20 cm$ and contains one or two intercalations of ash layers. The juvenile component is made up of subaphiric grey-blackish scoria lapilli; the lithic component mostly includes lava and subordinately sedimentary clasts (reddish clays), usually < 1 cm in size; loose crystals (feldspars, clinopyroxene and leucite) are rare. This deposit is exposed SE of the present caldera with a NW-SE dispersal axis and an inferred source area located inside the caldera. The overlying pumice fall subunit shows a maximum observed thickness of 50 cm and multiple grading, with a distinctive centimeter-thick ash layer interbedded. The juvenile component is made up of centimeter-sized, subaphiric, whitish pumice containing clinopyroxene, leucite and feldspars phenocrysts. The lithic

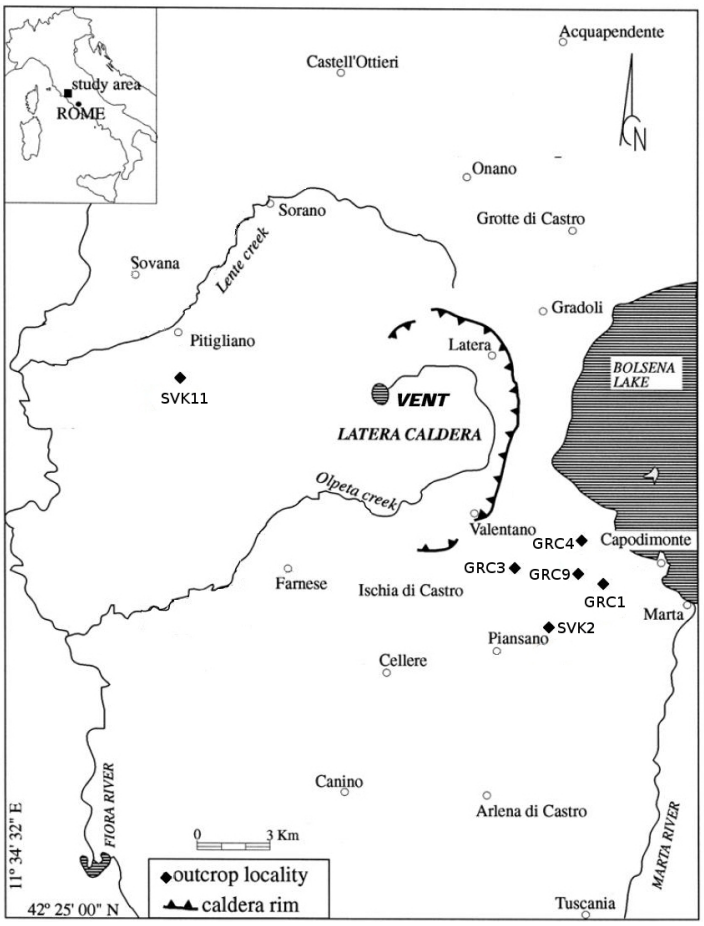

Figure 1: Location and geological sketch map of the Vulsini Volcanic District (Roman Province) which comprises the Latera caldera and the vent area inside. The black diamonds indicate the outcrops location

component is mostly represented by lava and subordinate sedimentary (red clays) centimeter-sized clasts. Loose feldspars, clinopyroxene and leucite crystals are also present. Also this deposit is distributed SE of the Latera Caldera, with a NW-SE dispersal axis and a common inferred source area as the preceding strombolian phase. The pumice fall subunit passes directly to an ash-dominated pyroclastic current deposit that shows a maximum observed thickness of about 3 m. In relatively proximal areas it is mildly to strongly lithified, and well-stratified due to the presence of ca. 30 cm-thick beds and plane-parallel to low-angle cross-lamination, with tractional features such as swarms and inversely graded layers of juvenile scoria/pumice lapilli (Fig. 2). The presence of abundant accretionary lapilli and vegetation marks, including leaves and tree molds (up to 30 cm across; Fig. 2), together with the ash-rich nature, is the most prominent deposit feature. The dominant ash component, as well as lapilli-sized clasts, are represented by grey-blackish scoria and subordinate whitish pumice; accessory lava fragments and loose crystals of feldspars, clinopyroxene and leucite are also present, while accidental lithics are absent. This deposit is axisymmetrically distributed all

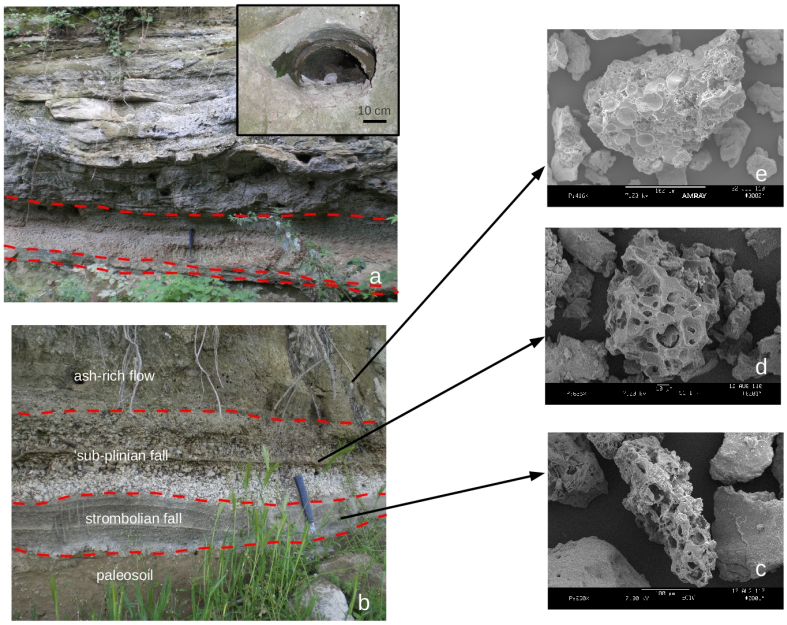

Figure 2: Field images of the lower part of the Grotte di Castro formation under study (a: locality 9, b: locality 3, Fig. 1); the top right inset in (a) shows an example of tree mold in the dune-bedded, accretionary-lapilli-bearing ash-rich surge deposits. c, d, e: representative SEM microphotographs of juvenile ash grains from the different eruption phases.

around the present Latera Caldera; outside the dispersal area of the underlying fallout horizons, it directly rests on top of a decimeter-thick paleosoil. An up to 60cm thick paleosoil separates the study succession from the upper member of the GRC formation (Vezzoli et al., 1987).

Bulk chemical compositions of juvenile clasts (Table 1) were determined by microprobe analyses of homogeneous glass beads, obtained by grinding and fusing individual clast samples. The composition of both strombolian scoria and juvenile lapilli from the ash-rich pyroclastic current deposits plots in the shoshonite field of the TAS diagram, while the plinian pumice is phonolitic in composition. Chemical bulk compositions (Tab.1), determined by microprobe analysis of a homogeneous glass bead, obtained by grinding and fusing the rock sample, plot in the shoshonitic TAS area (strombolian scoria fall, ash-rich pyroclastic current) and in the phonolitic area (plinian pumice fall).

3.1.2 *Sovana*

The Sovana eruption (SVK) products are widely exposed around the present Latera Caldera and are probably related to a major stage of caldera collapse (Palladino et al., 2010). The SVK eruption succession rests on top of a dark brown paleosoil, up to 1 m thick, developed on top of the Farnese Eruptive Unit (Vezzoli et al., 1987). The SVK shows an unusually high degree of magma fragmentation at the eruption onset, leading to the emplacement of widespread ash from a

Sample	GRC-a	GRC-b	GRC-c	SVK_1	C.I.
SiO_2	51.97	60.07	51.97	58.69	61.54
TiO−2	0.95	0.46	0.83	0.54	0.29
Al_2O_3	17.69	18.84	17.70	18.49	18.74
FeO	8.61	3.79	8.24	3.46	3.30
MnO	0.17	0.20	0.07	0.17	0.18
MgO	4.39	0.81	4.33	0.54	0.24
CaO	9.29	3.30	8.88	2.61	1.79
Na_2O	3.86	3.14	2.52	2.39	6.16
K_2O	2.10	9.05	4.23	9.29	7.09
P_2O_5	0.61	0.15	0.40	0.07	0.06
Cl	0.04	0.05	0.03	-	0.21
F	0.06	0.01	0.23	-	0.36
SO_3	0.03	0.08	0.07	-	-
Tot.	99.76	99.95	99.50	96.25	99.96

Table 1: Microprobe chemical bulk analysis of the study deposits. GRC = Grotte di Castro; -a: strombolian scoria fall; -b: plinian pumice fall; -c: ash-rich pumice flow; SVK. = Sovana, ash-rich flow; C.I. = Campanian Ignimbrite, obsidian sample used in the experiments. $_1$: XRF analysis from Palladino and Taddeucci (1998)

dilute, turbulent pyroclastic current (BUS; Palladino and Taddeucci, 1998; Taddeucci and Palladino, 2002), followed abruptly by "conventional", coarse pumice-bearing pyroclastic flow deposits (Fig. 3; Sparks, 1975; Palladino and Valentine, 1995) and associated proximal lithic-rich breccias. The BUS is a decimeter-thick (maximum observed thickness 85cm), loose to mildly consolidated, pale yellow to greenish ash-rich bed, enclosing sparse, up to centimeter-sized, whitish, subaphiric (sanidine-bearing) pumice clasts and accretionary lapilli. The only deposit structures are subtle clast grading and stratification imparted by swarms of fine pumice and accretionary lapilli and/or abrupt grain size changes. Vegetation casts or charred wood are absent. The absence of thermal effects on the paleosoil and the occurrence of accretionary lapilli suggest a low emplacement temperature. The BUS mantles the gently sloping pre-eruptive surface with remarkable continuity over a nearly circular area outside the present-day Latera Caldera, as far as 15 km from the caldera rim. A conservative estimate of the deposit volume, based on the isopach distribution in the outcrop area, yields 0.4 km^3 (Palladino and Taddeucci, 1998). The inferred vent location is within the southwestern part of the present caldera area, as for the following co-eruptive SVK deposits. The BUS outcrop area coincides with that of the overlying pyroclastic flow deposit, suggesting that it was preserved due to the immediate emplacement of co-eruptive products. The overlying pyroclastic flow deposit, distributed all around the present caldera, is meter-thick, matrix-supported, massive and poorly sorted, showing normal and inverse coarse-tail grading

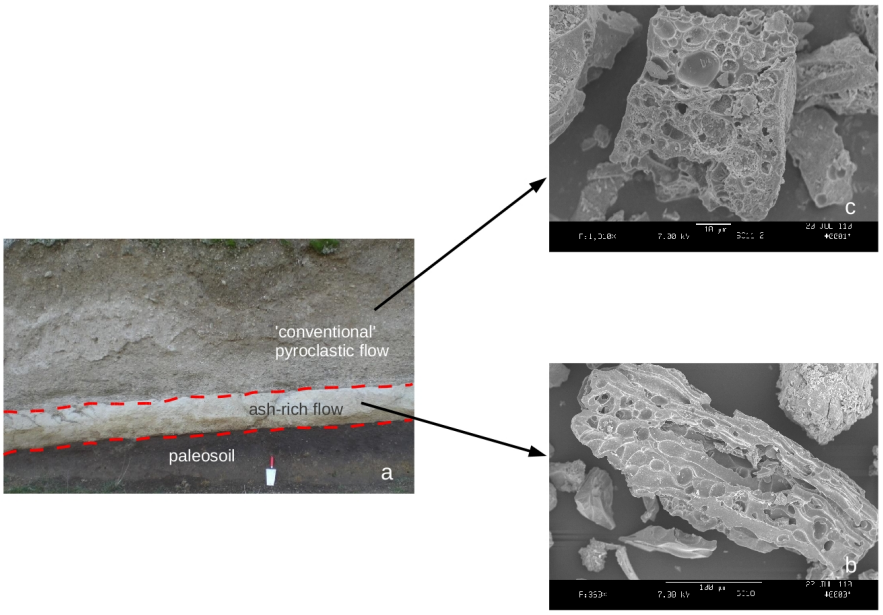

Figure 3: a: Field image of the lower part of the Sovana eruption succession under study (locality 2, Fig. 1). b, c: representative SEM images of ash grains from the two eruption phases.

of lithic and pumice clasts, respectively (Palladino and Valentine, 1995). The maximum observed thickness is up to 15 m in the southern sector of the Latera volcano and 5 m in the northern part. The juvenile component is made up of whitish/light grey to blackish pumice lapilli and blocks, containing sanidine, leucite, clinopyroxene and biotite phenocrysts, also present in the ash matrix. The abundant lithic component is represented by a variety of centimeter- to decimeter-sized volcanic and sedimentary clasts, which locally concentrate in breccia layers. Regardless the variable textural appearance, the bulk chemical composition of juvenile pumice is phonolitic throughout the SVK succession (Fig.1 Vezzoli et al., 1987; Palladino and Taddeucci, 1998).

3.2 CAMPANIAN IGNIMBRITE

Two major explosive eruptions, the Campanian Ignimbrite (CI) and the Neapolitan Yellow Tuff, occurring respectively at 39 and 12 ka, produced a cumulative magma mass transport to the surface greater than 300 km^3, and make the Campi Flegrei Volcanic Field (fig. 4) one of the riskiest in the world (references in De Vivo et al. (1976)). The last recorded eruption occurred in 1538 A.D. originating a small tuff cone called Monte Nuovo. This eruption and the recent unrest and seismic episodes associated with the current hydrothermal and fumarolic

activity testify that the magmatic system is still active (De Vivo et al., 1976; De Natale, 2006; Trigila et al., 2008).

CI is the largest pyroclastic deposit in the Mediterranean area (Barberi et al., 1978). It covers an area of about 30000km^2, with an estimated volume of erupted magma of about 150km^3 (DRE; Civetta et al., 1997). The eruption generated a compositionally zoned, basal plinian fall deposit and at least three pyroclastic flow units (Fisher et al., 1993; Rosi et al., 1996). In proximal areas, four breccia units (Breccia Museo) have been recognized and correlated to the caldera forming event (Rosi et al., 1996). The obsidian sample used for the experimental study in the present work has been collected within the Campanian Ignimbrite eruption succession exposed at Punta della Lingua, Procida Island (Central Italy) (fig.5, 6). On Procida island, as it occurs for proximal CI exposures on the mainland (e.g., Camaldoli Hill), facies architecture includes welded spatter flow, coarse lithic-rich breccia and ash-pumice flow deposits, typically of relatively proximal deposits from a caldera-forming eruptive event. In particular, at Punta della Lingua, the CI overlies an unconformity that cuts into a yellow, stratified pyroclastic deposit, lithified due to vapour phase crystallization of zeolite minerals, part of local tuff cone activity. The local CI eruptive succesion (fig.5, 6) includes i) basal strongly welded spatter flow deposit (ca. 2.5 m thick); ii) massive, spatter-bearing, coarse lithic-rich breccia (>7 m thick); iii) clast-supported, coarse lapilli- to boulder-sized lithic-rich breccia with a fines-poor pumiceous matrix, also containing isolated meter-sized black spatter blocks and diffuse obsidian clasts, interpreted as a 'lag breccia' which marks the eruption climax concomitant to the onset of caldera collapse; iv) massive, poorly consolidated, ash and pumice flow deposits with degassing pipes (>10 m thick). The vertical and lateral facies transitions are marked by gradually changing proportions of spatter, pumice and lithic components.

The obsidian block used in the present work has been collected within the 'lag breccia' deposit. It shows millimetric euhedral sanidine phenocrysts (up to $10-15\%$ of the volume) commonly associated with augitic pyroxene, corroded bytownite, euhedral andesine, spinel, biotite and apatite (all together $5-8\%$ of the total volume) . Table 1 shows the composition of the studied sample, falling in the field of the Campanian Ignimbrite products (Fowler et al., 2007).

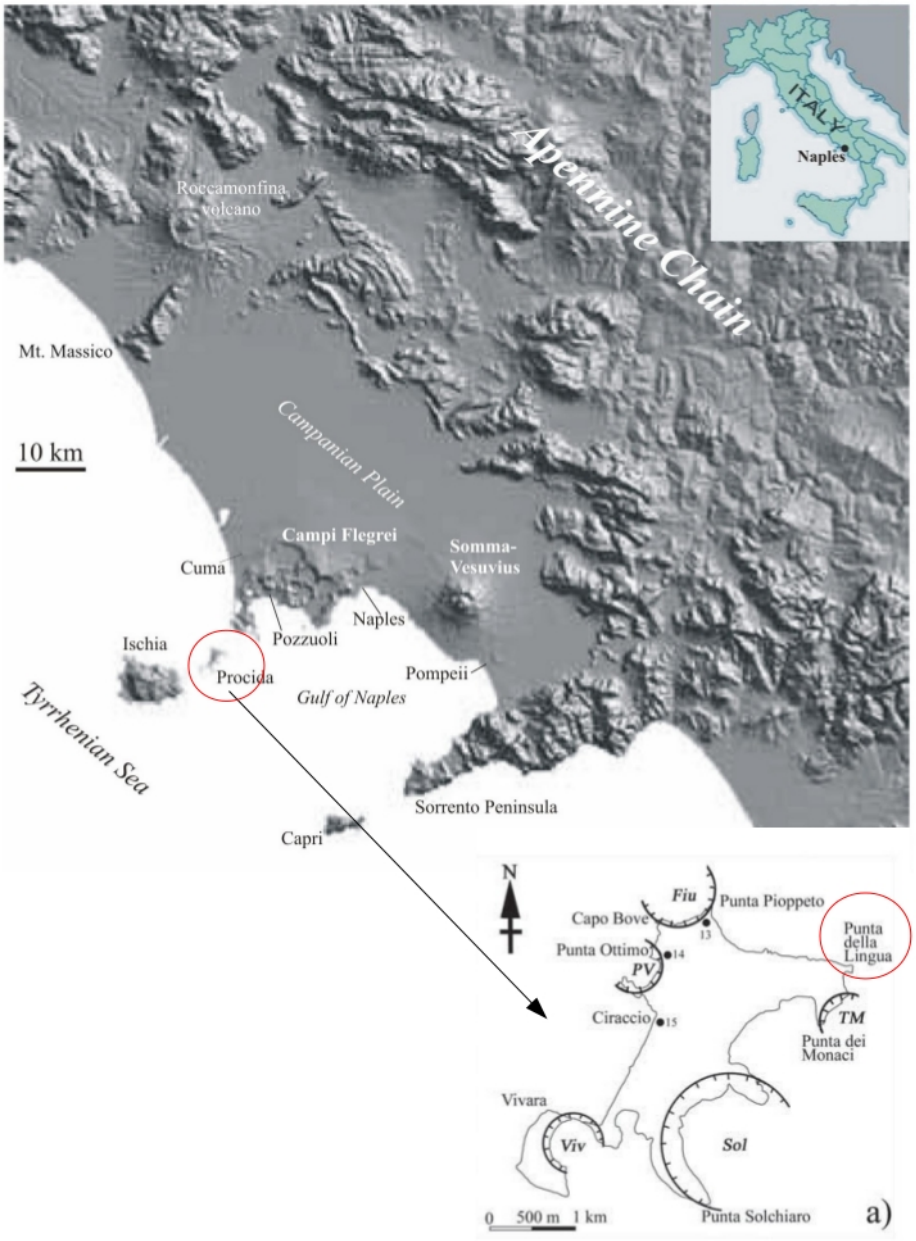

Figure 4: Location and geological sketch map of the Campi Flegrei volcanic field; a) Procida island and Punta della Lingua outcrop (image modified from Palladino et al., 2008b)

Figure 5: Procida Island, Punta della Lingua. Outcrop of the strongly welded spatter-flow deposit passing upward to the coarse lithic-rich breccia deposit, emplaced during the early phases of the Campanian Ignimbrite eruption in a proximal (near-vent) setting.

Figure 6: Procida Island, Punta della Lingua. Close-up of the lithic-rich breccia enclosing coarse lapilli- to boulder-sized lithic clasts representative of virtually all sedimentary and igneous rock types from the wall rocks of the crustal magma reservoir and feeder conduits (beach balloon for scale).

4

METHODS

The Gas bubble nucleation problem has been studied, initially, from a theoretical-numerical perspective. The role of surface tension in the theory of nucleation processes has been analysed. The surface tension has been calculated using a method based on statistical thermodynamics. Laboratory experiments, using a novel experimental facility, have been performed in order to verify the effect of surface tension on bubble nucleation. Finally a new method to take 3D measurements (Proussevitch et al., 2011) has been applied to natural samples, in order to characterize the vesiculation (in terms of nucleation and growth) of ash-rich eruptions and correlate the nucleation mechanism to magma fragmentation leading to extensive ash formation during volcanic eruptions.

4.1 THE STATISTICAL THERMODYNAMICS APPROACH TO SURFACE TENSION

Quantity	Symbol	Units
Characteristic volume	$\dot{v}$	l^3/mol
Chemical potential	μ	E/mol
Density	ρ	m/l^3
Gas constant	R	E/mol*T
Grand Thermodynamic Potential	Δa	E/l^3=F/l^2
Influence parameter	k	dimless
Interaction energy term	$\dot{e}$	E/mol
Molar mass	M	m/mol
molar volume of the mixture	v_{mix}	l^3/mol
Number of lattice sites occupied by a molecule	r	dimless
Partial density	ρ_i	mol/l^3
Pressure	P	F/l^2
Pure component parameter density	$\dot{\rho}$	m/l^3

Table 2: Quantities used in the model. dimless=dimensionless, E=energy, F=force, l=length, mol=mole, T=temperature.

Using a procedure similar to that proposed by Cahn and Hilliard (1959), Poser and Sanchez (1981) developed a model, based on statistical thermodynamics, to compute the surface tension of binary mixtures, considering the change of the partial densities of the two components of the mixture within a planar interface. This model requires an equation of state (hereafter EOS) of the binary mixture. The most popular EOS for this kind of calculation is the Sanchez-Lacombe equation of state (SL EOS; Enders et al., 2005; Poser and Sanchez, 1981; Sanchez and Lacombe, 1976).

The model involves the following steps: i) determining the EOS of the pure components (i.e. magma and water); ii) determining the EOS of the binary

Quantity	Symbol	Units
Pure component parameter pressure	$\dot{P}$	F/l^2
Pure component parameter surface tension	$\dot{\sigma}$	E/l^2
Pure component parameter temperature	$\dot{T}$	T
Reduced characteristic volume	$\tilde{\sigma}$	dimless
Reduced density	$\tilde{\rho}$	dimless
Reduced influence parameter	$\tilde{k}$	dimless
Reduced pressure	$\tilde{P}$	dimless
Reduced surface tension	$\tilde{\sigma}$	dimless
Reduced temperature	$\tilde{T}$	dimless
Surface tension	σ	E/l^2
Temperature	T	T
Volume fraction	ϕ	dimless
Weight fraction	w	dimless

Table 3: Quantities used in the model. dimless=dimensionless, E=energy, F=force, l=length, mol=mole, T=temperature.

mixture; iii) calculating the surface tension of the binary mixture. Finally (iv), I entered the surface tension, so calculated, into the Classical Nucleation Theory to calculate the nucleation rate

i) The starting step in developing the model is determining the EOS of the pure components, i.e. magma and water. The Sanchez-Lacombe equation of state (SL EOS; Sanchez and Lacombe, 1976) is a lattice fluid equation, calibrated on experimental data, describing density-dependent phenomena

$$\tilde{\rho^2} + \tilde{P^2} + \tilde{T^2}\left[\ln 1 - \tilde{\rho} + (1 - \frac{1}{r}\right] = 0 \tag{4.1}$$

where

$$\tilde{\rho} = \frac{\rho}{\dot{\rho}}; \tilde{P} = \frac{P}{\dot{P}}; \tilde{T} = \frac{T}{\dot{T}}; \tag{4.2}$$

are respectively the reduced parameters for density, pressure and temperature. The pure components parameters, $\dot{\rho}$, $\dot{P}$, $\dot{T}$, are obtained by fitting the EOS equation to experimental data of temperature and pressure dependence of the density and equilibrium phases. To this end, I realized a best fit algorithm that uses the MATLAB function fmincon (optimization toolbox) to minimize the χ^2 per degrees of freedom (List. 1). The following relations characterize the parameters:

$$\dot{\epsilon} = R\dot{T}; \dot{v} = \frac{R\dot{T}}{\dot{P}}; r = \frac{M\dot{P}}{R\dot{T}\dot{\rho}} \tag{4.3}$$

where R is the gas constant, $\dot{\epsilon}$ represents the interaction energy term, $\dot{v}$ the characteristic volume and $\dot{r}$ the number of lattice sites occupied by a molecule.

The parameters of the pure magma component are calculated fitting (4.1) to the empirical formula proposed by Lange and Carmichael (1990) for the dependence of density on pressure and temperature (Fig. 7; Tab. 5; List. 1). This

formula allows to calculate the volume of an anhydrous silicate liquid taking into account the experimental thermal expansion and compressibility of oxide components, as well as the chemical bulk composition (Lange and Carmichael, 1990). In this case, I used the trachytic composition of the experimental sample (Tab.4.19).

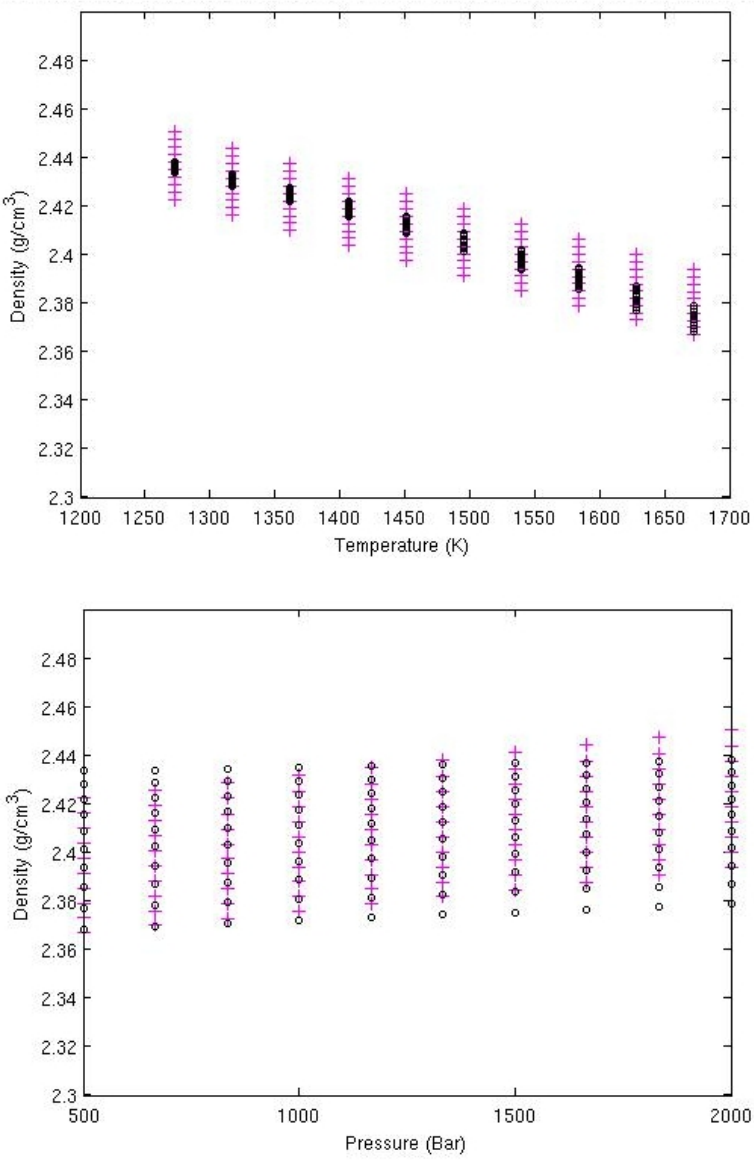

Figure 7: Pressure/temperature dependence of the trachyte density at various temperature/pressure. Cross symbols are the data from the empirical formula proposed by Lange and Carmichael (1990) in the temperature range 1000-1400 ◦C /pressure range 500-2000 bar. Circles are the values calculated by the SL EOS.

The parameters of pure water are reported in Machida et al. (2010), who propose pure parameters different from the classical ones (Sanchez and Lacombe, 1976), by taking into account the temperature dependence of hydrogen bonding

and ionic interactions (Tab. 4). In their approach $\dot{\epsilon}$ is not treated as a constant, but is temperature dependent

$$\epsilon(\dot{T}) = \epsilon_0 \frac{\alpha T}{1 + \alpha T} \tag{4.4}$$

The value for parameter α represents the temperature dependence and ϵ_0 is the asymptotic value of the interaction energy.

The EOS of the pure components are then used to calculate the influence parameters of magma (k_A) and water (k_B), fitting to the experimental data of the surface tension of the pure components, i at a given temperature, eq. (4.5), in the reduced form (Poser and Sanchez, 1979; List. 3):

$$\tilde{\sigma} = 2 \int_{\tilde{\rho}_l}^{\tilde{\rho}_g} (\tilde{k}_i \Delta\tilde{a})^{\frac{1}{2}} d\tilde{\rho}_i; i = A, B \tag{4.5}$$

$$\tilde{\sigma} = \sigma/\dot{\sigma}; \dot{\sigma} = \dot{\epsilon}/\dot{v}^{\frac{2}{3}}; \tag{4.6}$$

$$\tilde{k} = k/\dot{v}^{\frac{2}{3}}; \tag{4.7}$$

The Grand Thermodynamical potential $\tilde{\Delta}a$ represents the difference between the actual free energy at the interfacial region of the inhomogeneous system and that which would exist assuming the system homogeneous. It is given by:

$$\Delta\tilde{a} = [\tilde{\rho}\tilde{\mu}(\tilde{\rho}, \tilde{P}_{eq}) - \tilde{\rho}\tilde{\mu}_{eq}]; \tag{4.8}$$

The equilibrium chemical potential is calculated imposing the equilibrium condition:

$$\mu_l(P) = \mu g(P); \tag{4.9}$$

where the P equating the potentials represents the equilibrium pressure P_{eq} for a fixed temperature. The chemical potential for a pure component is given by (Poser and Sanchez, 1979):

$$\tilde{\mu} = -\tilde{\rho} + \tilde{P}\tilde{v} + \tilde{T}[(1/\tilde{\rho} - 1)\ln(1 - \tilde{\rho} + \frac{1}{r}\ln(\tilde{\rho})]; \tag{4.10}$$

Pure magma (anhydrous) has no detectable surface tension, so a standard value for real polymers (Enders et al., 2005) has been assumed (5).

The influence parameter k_B for water has been calculated fitting the experimental data of liquid-gas water surface tension reported in (Kahl and Enders, 2000; 8; Tab. 4).

ii) The EOS of the pure components are then used to calculate the EOS of the binary mixture through the following mixing rules (Enders et al., 2005):

$$\dot{P} = \sum_i \sum_j \phi_i \phi_j P_{ij}; \tag{4.11}$$

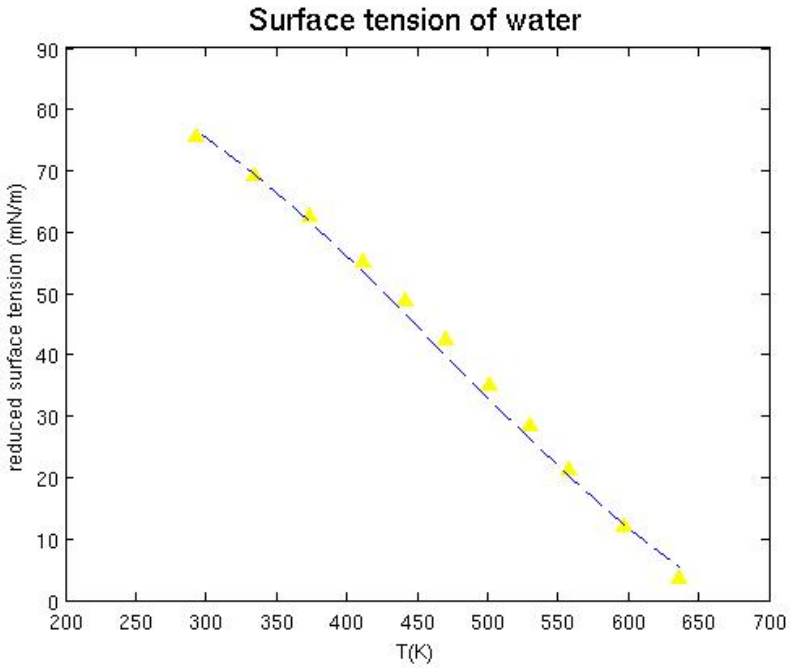

Figure 8: Temperature dependence of the water surface tension. Triangle symbols are experimental data from Kahl and Enders (2000). The dashed line represents the surface tension calculated by the model

Water		
$1/\alpha$	[K]	207.0
ϵ_0	[J/mol]	7447
$\dot{v}$	[cm^3/mol]	2.614
r	[adim]	5.823
$\tilde{k}_{magma}$	[adim]	0.91

Table 4: Pure component parameters ($1/\alpha, \epsilon_0, \dot{v}, r$) and influence parameter ($\tilde{k}_{water}$) of water proposed by Machida et al. (2010) to take into account the temperature dependence of hydrogen bonding and ionic interactions. In the new form $\dot{e}$ is not treated as a constant but the temperature dependence is considered.

Table 5: Pure component parameters: $\dot{\rho}, \dot{P}, \dot{T}$; influence parameter of the trachytic magma: ($\tilde{k}_{magma}$). Binary interaction parameter of the binary system trachyte-water: $k_{1,2}$

$\dot{\rho}$[kg/m^3]	$\dot{P}$[MPa]	$\dot{T}$[K]	$\tilde{k}_{magma}$	$k_{1,2}$
2473.1	4915.6	4449.1	0.3	-0.0355

$$\dot{P_{AB}} = (1 - k_{AB})\sqrt{\dot{P_A}\dot{P_B}}; \tag{4.12}$$

$$\dot{T} = \dot{P}\sum_i \frac{\phi_{i,0}\dot{T_i}}{\dot{P_i}}; \tag{4.13}$$

$$\frac{1}{r} = \sum_i \frac{\phi_{i,0}}{r_{i,0}} \tag{4.14}$$

$$\phi_{i,0} = \frac{\phi_i \dot{P}_i / \dot{T}_i}{\sum_j \phi_j \dot{P}_j / \dot{T}_j}; \tag{4.15}$$

$$\phi_i = \frac{w_i/\rho_i}{\sum_j w_j/\rho_j}; \tag{4.16}$$

$$\nu_{mix} = \sum_i \phi_i \dot{\nu}_i; \tag{4.17}$$

where ν_{mix} is the molar volume of the mixture, ϕ is the volume fraction and w the weight fraction. The binary interaction parameter k_{AB} is determined so as to minimize the relative deviations between experimental and calculated values of solubility of water in magma (Tab. 5), using the same kind of Matlab algorithm described in i)(List. 2). The experimental solubility data for the trachytic system are reported in De Rita et al. (1976) and Di Matteo et al. (2004). The solubility (Fig. 9) is calculated using the EOS for the binary mixture and the same equilibrium criterion of (4.9) extended to a binary system that reads:

$$\mu_{Bl} = \mu_{Bg}; \tag{4.18}$$

where the chemical potential of B (i.e. water) is calculated respectively in the liquid and in the gas phase. The equation for chemical potential of water in the binary mixture is given by:

$$\begin{aligned} \mu_i = RT(\ln\phi_i + (1 - \frac{r_i}{r_j})\phi_j + r_i\tilde{\rho}((\dot{P_A} + \dot{P_B} - 2\tilde{P_{A,B}})/(\dot{P_A}\tilde{T_A}))\phi j^2) \\ + r_A RT(-\tilde{\rho}/\tilde{T_A} + \tilde{P_A}/(\tilde{\rho}\tilde{T_A}) + (1/\tilde{\rho})((1-\tilde{\rho})\ln(1-\tilde{\rho}) + (\tilde{\rho}/r_A)\ln(\tilde{\rho}))); \end{aligned} \tag{4.19}$$

where $\tilde{\rho}$ is the reduced density of the binary mixture.

iii) The interfacial tension (σ) between the two fluid phases (liquid and gas), is given by (Poser and Sanchez, 1981) :

$$\sigma = 2^{\frac{1}{2}} \left[\sqrt{k_A} + \sqrt{k_B}\frac{\Delta\rho_B}{\Delta\rho_A}\right] \int_{\rho_{AII}}^{\rho_{AI}} \Delta a^{\frac{1}{2}} d\rho_A \tag{4.20}$$

where ρ_{AI} and ρ_{AII} are the partial densities of component A in the coexisting liquid and gas phases. The partial volume density is given by:

$$\rho_{iJ} = \phi_{iJ}\frac{\tilde{\rho}}{\nu_{mix}}; i = A, B; J = I, II; \tag{4.21}$$

where $\tilde{\rho}$ is the reduced density of the binary mixture, ϕ_{iJ} is the volume fraction of component i in the J phase and ν_{mix} is the molar volume of the mixture. $\Delta\rho A$ and $\Delta\rho B$ in equation 4.20 are the differences in density of a component

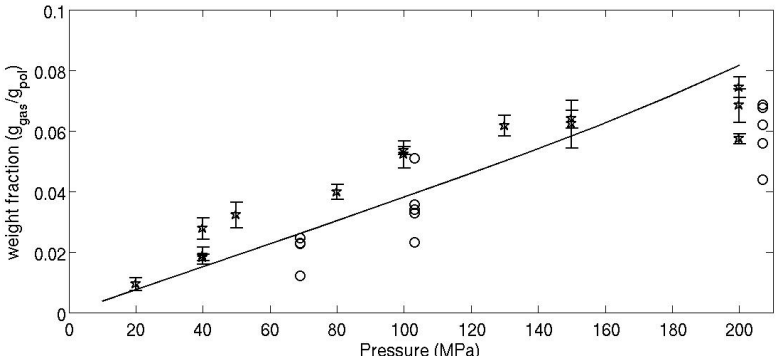

Figure 9: Solubility curve for the trachyte of Phlegrean Fields. Solid line represents the solubility calculated by the SL EOS. The stars are the experimental data from Di Matteo et al. (2004), the open circles from De Rita et al. (1976)

between the two bulk phases (liquid and gas). In this case, the component A (i.e. magma) has a negligible vapour pressure, thus only the component B (i.e. water) is present in both phases. All these variables are calculated by the equation of state (EOS) of the binary mixture. k_A and k_B are the influence parameters of the fluid, estimated basing on the experimental surface tensions of the pure components at a given temperature. The Grand Thermodynamic Potential of the binary mixture is given by:

$$\Delta a = \rho_A(\mu - \mu_{eq}); \tag{4.22}$$

where μ represents the chemical potential of the homogeneous system and μ_{eq} the equilibrium chemical potential, both of them calculated by the EOS.

Using (4.20; List. 4) the free energy barrier within the interface is calculated and the surface tension of the binary mixture estimated (Fig. 14).

iv) The surface tension so obtained (Fig. 14, 15), a function of pressure, has been used to calculate the homogeneous nucleation rate using Classical Nucleation Theory (CNT; Landau and Lifshitz, 1980). According to CNT the nucleation rate, i.e. the number of bubbles nucleated in 1 s in 1 m^3, is given by:

$$J = \frac{2n_0 D v_w}{a_0}\left(\frac{\sigma}{kT}\right)^{\frac{1}{2}} \exp\frac{-16\pi\sigma^3}{3kT\Delta P^2} \tag{4.23}$$

where n_0 (10^{27} molecules/m^3; Mangan and Sisson, 2005) is the concentration of potential sites, taken as the number of water molecules in the melt, v_w ($10^{-29} m^3$) is the volume of a water molecule , a_0 (10^{-9} m; Mangan and Sisson, 2005) is the distance between neighbouring water molecules, D the diffusivity of a trachyte (Freda et al., 2003), k the Boltzmann constant, T the temperature, ΔP the decompression and σ the surface tension.

4.2 NUCLEATION EXPERIMENTS USING A MINI INTERNAL HEATED PRESSURE VESSEL

The decompression experiments were performed using the HP16/60 Miniclave (Fig. 10) at the Dipartimento di Scienze della Terra, Università degli Studi di

Roma Sapienza. The HP16/60 Miniclave is novel low-cost experimental facility, very simple to operate and allowing a fast quenching of the sample. This is an internally heated pressure vessel (IHPV) achieving a maximum pressure of 500 MPa and a maximum temperature of 1200 ∘C. Compared to the 'classical' IHPV, the HP16/60 is much more manageable, with a size of 32X10 cm and a weight of 8 Kg. The rock-type used in this work is an obsidian sample collected from the Lag Breccia Unit, in the lower part of the Campanian Ignimbrite pyroclastic succession (Phlegrean Fields, Central Italy), exposed at Punta della Lingua, Procida Island (location in Chap. 3 Fig. 4; chemical analysis in Chap. 3 Tab. 1). Platinum tubes (ca. ≈ 3mmX18mm) were filled with the powder of the sample, hydrated with a variable percent content of distilled water and finally welded leaving enough void space inside the capsule to allow for the gas expansion. The reported experiments refer to 12 decompression runs performed at different initial pressures, combined with 3 different decompression values (Tab. 6). Each experiment started leaving the sample for 1 hour at the P-T conditions of interest. The capsule was then instantly ($< 2s$) decompressed isothermally and fast-quenched ($< 5s$) switching off the furnace and twisting it to the vertical position. The vessel thermocouple is tight to the sample wall to ensure that the temperature value read on the display represents the actual temperature experienced by the sample. The fast decompression of the miniclave, allows us to consider the decompression leading to bubble nucleation as the difference between the initial and the final pressure value. The time before quenching is short enough to consider bubbles growth negligible, according to the typical Delay Time, i.e. the time before growth process starts (Proussevitch and Sahagian, 1998). The water content for each experiment exceeds the reference solubility (De Rita et al., 1976; Di Matteo et al., 2004) at the pressure of interest. The super-liquidus pressure-temperature (P-T) of the experiments have been determined from isobaric simulations using the MELTS code (Ghiorso and Sack, 1995). Four Isobaric quenching experiments have been performed in order to verify the P-T simulations. The bubbles generated experimentally have been observed by scanning electron microscope (SEM) FEI Quanta 400 equiped with EDAX Genesis microanalysis system at at the Dipartimento di Scienze della Terra, Università degli Studi di Roma Sapienza. Finally, the images so obtained have been processed to determine Bubble Size Distributions (BSD) using the technique reported in Proussevitch et al. (2007). The BSD can give useful information on vesiculation processes in terms of growth and nucleation. In particular, the nucleation process has been evaluated through the Bubble Number Density (BND) and the amount of water dissolved in the sample after the experiments determined by a CE CHN-1110 gas chromatographic elemental analyser.

4.3 NATURAL SAMPLES ANALYSIS BY STEREO-SCANNING ELECTRON MICROSCOPY (SSEM)

4.3.1 *Materials and methods*

Preliminary investigations by Scanning Electron Microscope (SEM) were performed on ash- and lapilli-size juvenile pyroclasts in order to detect the magmatic

Figure 10: the HP16/60 Miniclave in use in the High Pressure - High Temperature laboratory of the Department of Earth Science of the University of Rome 'Sapienza'

Run	H_2O [wt%]	T [°C]	P_i [bar]	$C(P_i)$ [wt%]	P_f [bar]	$C(P_f)$ [wt%]	ΔP [bar]	H_2O_{dis} [wt%]	BND $n_{bubbles}/m^3$
SC19	4.39	1000	851	3.8	725	3.4	126	3.24	$1.1*10^{14}$
SC18	4.15	970	800	3.6	625	3.0	175	1.98	$1.7*10^{14}$
SC17	4.39	1000	875	3.9	585	2.8	290	2.61	$1.8*10^{14}$
SC42	3.36	990	590	2.9	180	1.1	410	2.52	$1.8*10^{14}$
SC49	3.73	985	572	2.8	255	1.3	317	2.79	$5.5*10^{13}$
SC44	4.73	985	625	3.0	408	2.1	217	2.52	$5.4*10^{13}$
SC55a	6.62	985	1190	4.8	940	4.0	250	4.68	$1.7*10^{14}$
SC56b	6.57	980	1250	5.0	950	4.0	300	4.95	$1.7*10^{13}$
SC1	3.43	984	578	2.8	578	2.8	0	-	$5.1*10^{13}$
SC2	4.55	970	800	3.6	800	3.6	0	-	$2.0*10^{13}$
SC3	4.07	1002	873	3.9	873	3.9	0	-	$4.5*10^{13}$
SC4	5.37	1000	1240	5.0	1240	5.0	0	-	$3.9*10^{13}$

Table 6: Experimental results. T = temperature, P_i=initial pressure, P_f=final pressure, C= solubility (De Rita et al., 1976; Di Matteo et al., 2004), ΔP=decompression, H_2O_{dis}=dissolved water measured by gas cromatographic elemental analyser.

vs. hydromagmatic fragmentation style, according to widely accepted particle morphoscopy criteria (Heiken and Wohletz, 1985; Dellino and La Volpe, 1996a,b; Polacci et al., 2003; Rust and Manga, 2002). Then a method to determine the Bubble Size Distributions (BSD) using a novel application of the Stereo-Scanning

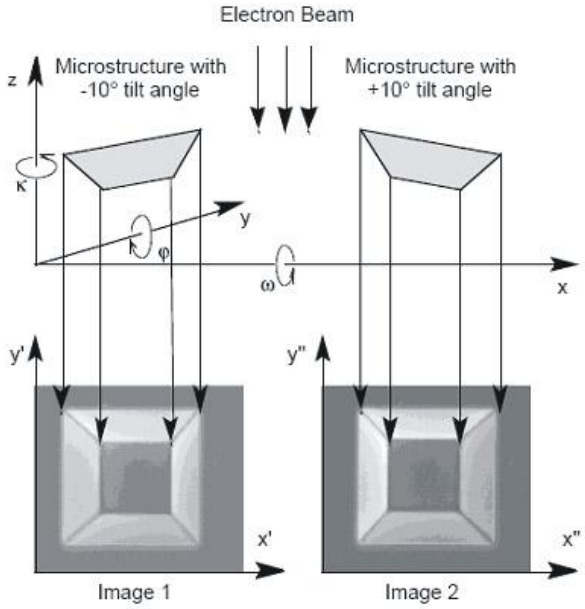

Figure 11: The tilting capability of the SSEM allows capturing two images of the sample with different tilt angle.

Electron Microscopy (SSEM) Technique (Proussevitch et al., 2011) has been tested on juvenile ash-sized pyroclasts from the same samples. The analysis were performed at the Instrumentation Center of the University of New Hampshire (NH, USA). The 125-250 µm grain-size class was chosen on purpose as the best compromise between the need of a good representativity of BSD and to avoid a significant interference of post-fragmentation vesiculation of pyroclasts. The technique is based on stereo-pair imaging of ash fragments by scanning electron microscopy with sample tilting capabilities SSEM (fig.11). The images so acquired can be used to create a digital elevation model (DEM) (fig.12), or 'topography', of the particle surface that records the micron-scale curvatures of vesicle wall surfaces (fig. 13). This method allows 3D measurements of vesicles within a size range from one to over million cubic microns.

4.3.2 *Sample preparation*

Isolating representative ash grains from samples collected is a very subjective task dependent on the quality of samples. Ash grains collected here, particularly from the GRC samples, were often present in mildly consolidated/cemented state, with observed weathering in many isolated grains and in many cases visible vesicle portions being heavily obscured by the presence of adhering dust. So, the samples were initially dried in a standard oven at 60 ◦C for 24 hours, and subsequently immersed in water in a test tube and sonicated. Sonication, the technique of applying ultrasound, was found to be an effective technique to break apart cemented samples as well as clear the adhering dust and weathering products from obscured vesicles. I found that sonication at a low energy setting for approximately 10 minutes was effective in accomplishing the task without

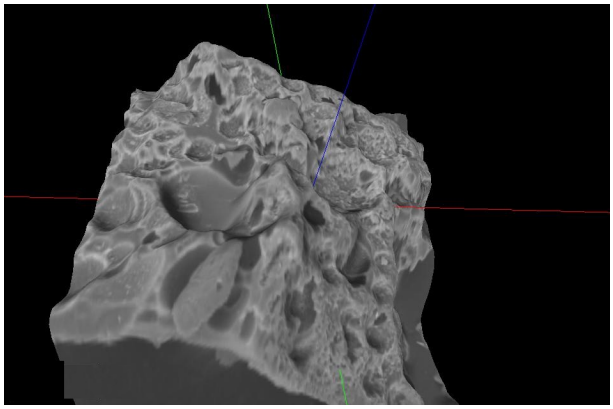

Figure 12: Topography of the particle surface obtained by the digital elevation model (DEM)

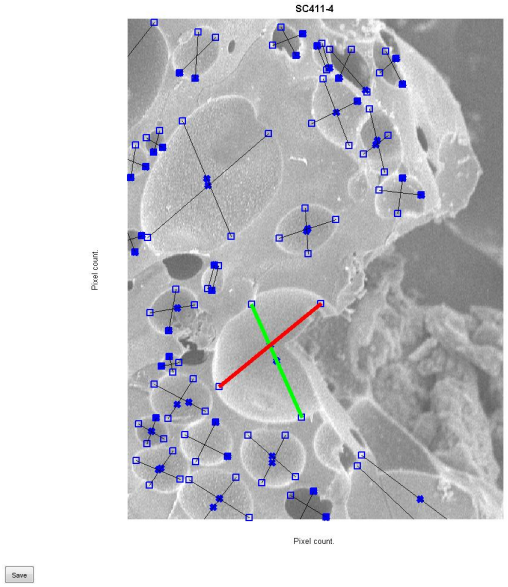

Figure 13: The Bubble Maker software allows the 3D measurement of the bubble.

degrading the ash grains. Sample stubs for SSEM analysis were prepared in a plastic container, using a gust of air from a compressed air canister to allow the ash grains to become airborne and adhere to the carbon tape on the stub. At this stage, with some experimentation I was able to obtain a statistically unbiased sample of vesicular ash grains. The stubs were then coated with Gold-Palladium (Au-Pd). During the SSEM image analysis I chose a minimum number of 5 clasts to analyse for each sample, representing a total of about 150-200 bubbles per sample, a number arbitrarily chosen to represent an unbiased and statistically significant population to obtain a BSD. Table 7 in the next chapter summarizes the samples examined from GRC and SVK eruptions.

4.3.3 *Data analysis*

Here I tested new software routines that enable judicious selection of vesicle surface positions, and a new approach to stereo image rectification yielding excellent results in reducing distortion for accurate DEM construction. In order to characterise the BSD of the ash samples, the data so obtained have been processed using the analytical and computational formulation described by Proussevitch et al. (2007). Polymodal BSD are treated as superposed mixtures of unimodal distributions. Each bubble subpopulation is characterised by a Number Density function, n(V), that is the concentration of bubbles of a certain size, V, per melt volume, and could be considered as a local bubble number density:

$$n(V) = N_{total}\tilde{f}V) \tag{4.24}$$

where $\tilde{f}(V)$ is the probability density function, and N_{total} is the total number of bubbles per unit volume of matrix (melt+crystals). Hence the bubble number density (BND) of a complex BSD is defined by the sum of the different N_{total} for each distribution mode. So defined, BND, for a given nucleation event, is a non-extensive quantity that remains invariant as bubbles grow, so that it is related only to the nucleation process. The probability density function is given by:

$$\tilde{f}(V) = \frac{dF(V)}{dV} \tag{4.25}$$

where F(V) is the probability to find a bubble of size between o and V. For number density histograms with ΔV bin size and i size classes, the function takes the discrete form:

$$n(V_i) = \frac{1}{V_m}\frac{n_i}{\Delta V} \tag{4.26}$$

In order to determine the appropriate continuous distribution (i.e., the probability density function; Eq. 4.25) to characterise a bubble population, it is necessary to find the function that fits best the histogram data. The Number Density function (Eq. 4.24), which combines BND and the probability density (Eq. 4.25), thus provides an overall characterization of the ash particle vesicularity, including information on bubble nucleation, growth and coalescence.

5 RESULTS

5.1 SURFACE TENSION AND BUBBLE NUCLEATION: NUMERICAL MODEL AND EXPERIMENTS

I find that surface tension strongly depends on pressure, decreasing from 60 mN/m at 10MPa to 10 mN/m at 200 MPa (Fig. 14). The order of magnitude is consistent with experimental data from different silicate systems(Fig. 15; e.g. Mangan and Sisson (2005, 2000); Bagdassarov et al. (2000); Epelbaum et al. (1973)).

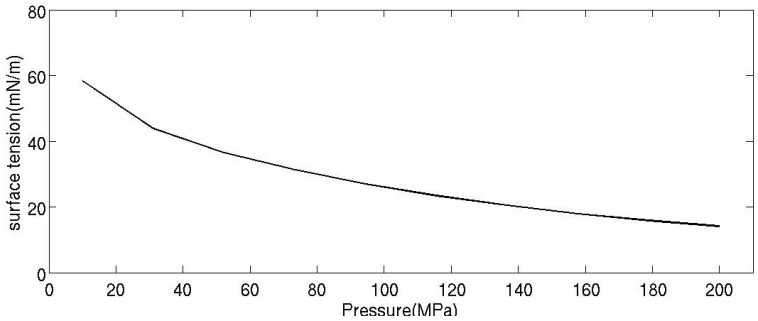

Figure 14: Surface tension calculated in this work.

The values obtained have been entered into the CNT to calculate the bubble nucleation rate as a function of pressure. The Figure 16 shows the relation between the decompression to nucleate bubbles and the nucleation pressure (i.e. the depth of the volcanic reservoir). The solid and dash lines are obtained by the model, the circles are the experimental data. The area between the two lines represents the interval of decompression in which the nucleation of the maximum number of bubbles commonly observed in natural (see the next section in this chapter) and experimental trachytic samples with rare crystals (this study: $10^{14} Bubbles/m^3$), can occur in a time scale between 1 day and 1 second. These two lines divide the explosive field (in red) from the effusive one (in blue). For example, starting from 100 MPa of pressure, the solid straight line of the decompression path enters into the explosive red area at $\approx$ 40 MPa of decompression. The key aspect of 16 regards the dependence of surface tension on pressure that makes nucleation at high pressures (i.e.$>$ 850bar) much more easy, in terms of decompression, than at lower pressures - i.e. nucleation at high pressure requires a lower decompression.

The isobaric quenching experiments show that, after one hour of homogenization, the sample is glassy and crystals-free. This is not bubble-free since there are micron-sized bubbles trapped in the melt. The Bubble Number Denisty (BND) calculated for these samples, ranging from $2 * 10^{13}$ to $5 * 10^{13}$ (Tab. 6), provides a base-line for the number of bubbles nucleated during decompres-

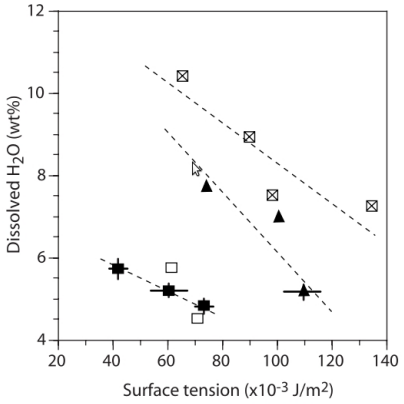

Figure 15: Surface tension vs dissolved water determined by Mangan and Sisson (2005) (solid squares), Mangan and Sisson (2000) (solid triangles), Bagdassarov et al. (2000) (crossed squares), Epelbaum et al. (1973) (open squares). In these cases the surface tension has been calculated as a function of the dissolved water, but the magma is not necessarily water-saturated and so the dependence on pressure cannot be write explicitly.

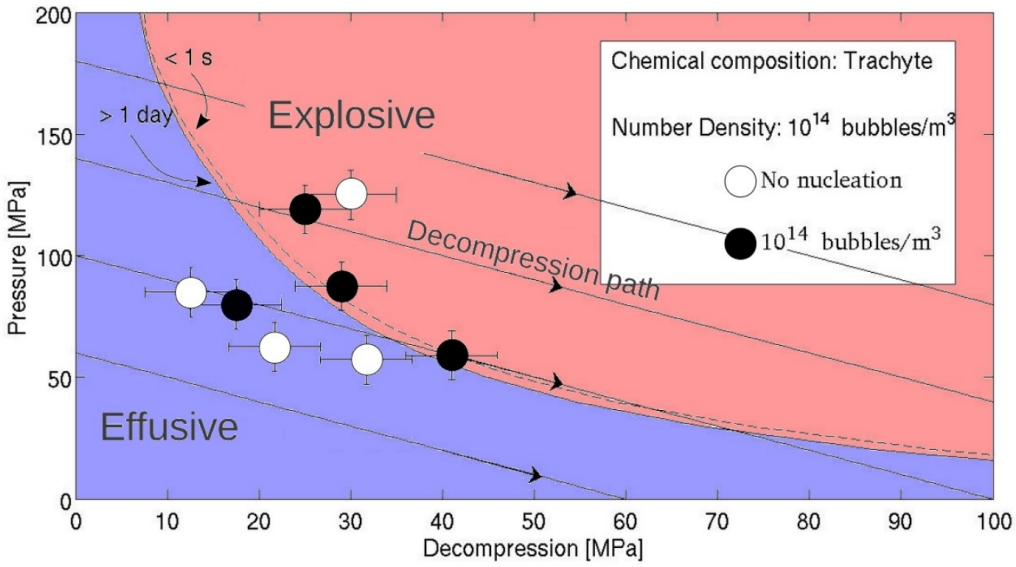

Figure 16: See the text for the explanation.

sion. The nucleation process can be considered negligible, if decompression experiments show a BND of the same order of magnitude of the base line (i.e. 10^{13}). Decompression experiments (Figure 16) show that bubbles nucleate when decompression ΔP, or supersaturation ΔS, exceeds $400 bar$, or $1.8 wt\%$

at $600bar$ of initial pressure and when exceeds $150bar$, or $0.4wt\%$, when the initial pressure is greater than $850bar$. The number of bubbles nucleated during the decompression is in the order of $10^{14}bubbles/m^3$ (Tab. 6). Bubbles are spherical, randomly distributed and only rarely attached to crystals. Mean bubble diameters are between $1-3\mu m$. Samples that nucleated bubbles during decompression (BND = $10^{14}bubbles/m^3$) have a dissolved water content closer to the predicted solubility at P_{final} , while the samples showing a negligible nucleation during decompression (BND = $10^{13}bubbles/m^3$) have a dissolved water content closer to the predicted solubility at $P_{initial}$ (Tab. 6).

The experiments (see fig.16) confirm that surface tension facilitates bubble nucleation at higher pressure. The decompression necessary to nucleate bubbles at high pressure ($> 850bar$) is at least three times lower than at low pressure ($< 600bar$; fig. 16).

5.2 BUBBLE NUCLEATION AND GROWTH IN THE ASH-RICH ERUPTIONS

Preliminary SEM analyses show that juvenile ash and lapilli from the strombolian fall and the ash-rich surge of GRC are moderately vesicular and characterised by spherical-elongated vesicles, while the subplinian fall is mostly characterised by highly vesicular, elongate tube pumices indicative of shear stress along the conduit (Palladino et al., 2008a). The SVK juvenile products are highly vesicular and dominated by slightly to highly elongate vesicles in both the study eruption phases. Elongated shape particles are likely related to the shear stress along the conduit. Particle morphoscopic and textural features (e.g., high degree of vesicularity, delicate-irregular contours and surfaces, absence of typical magma-water interaction signature, etc.) for both the eruptions (fig. 17, 18, 19, 20) do not provide evidence for significant hydromagmatic fragmentation ((Heiken and Wohletz, 1985; Dellino and La Volpe, 1996a,b; Palladino and Taddeucci, 1998; Polacci et al., 2003; Rust and Manga, 2002)), also for the ash-rich phases, thus suggesting a dominantly magmatic fragmentation mechanism.

Here we focus on the transitions from/to "conventional" to/from ash-rich phases in the study eruptions, i.e. from the subplinian fall to the subsequent ash-rich surge phase in the GRC and from the early ash-rich surge to the "conventional" ash-pumice flow in the SVK, which have been analysed through the BSD functions of ash-samples from each phase (Tab.7, fig.21). BND values are in the order of $10^{14}bubbles/m^3$ in the subplinian phase of the GRC eruption and 10^{13} to $10^{14}bubbles/m^3$ in the subsequent ash-rich surges. In the SVK eruption, BND values attain $10^{14}bubbles/m^3$ in the early ash-rich surge, whereas they are as high as $10^{15}bubbles/m^3$ in the subsequent conventional pyroclastic flow (Tab.7). The analysed samples show either unimodal or bimodal BSDs (fig.21), resulting from a single or two superimposed log-normal Number Density functions(eq.4.24 with variable BND and standard deviations. By comparing the BSDs of the "conventional" vs. the "ash-rich" phases, we note (Tab.7, fig.21): i) in both eruptions, the BND of "ash-rich" phases are ca. 1 order of magnitude lower than the associated "conventional" phases; ii) overall, BSDs are better sorted in the "ash-rich" samples than in the "conventional" one in the SVK case, while in the GRC case sorting differences are less significant; iii) in each eruption case,

the BSDs of associated "conventional" and "ash-rich" phases display a common main mode around a similar value of bubble size; iv) in the SVK case, the "conventional" phase (sample SVK11-2) shows a secondary, slightly subordinate, mode toward finer bubbles, while the "ash-rich" phase may show unimodal BSD (SVK2-8) or an additional minor mode toward coarser bubbles (SVK11-1); v) in the GRC case (where, we recall, the conventional and ash-rich phases are compositionally different), the ash-rich sample (GRC4-12) also shows a minor mode toward coarse bubbles (similar to ash-rich SVK11-1), which is not observed in the associated subplinian phase (GRC4-11); vi) the ash-rich layer immediately on top of the subplinian fallout (sample GRC1-R) shows a similar BSD shape as GRC4-12 for its secondary minor mode toward coarse bubbles, although with overall much smaller bubbles and relatively high BND, comparable to the subplinian phase.

Sample	Unit	Distrib.	Mode	Mean	Tot.N.Dens. [$bubbles/m^3$]	χ^2
SVK11-1	ash-rich flow	log-normal	bimodal	$\frac{-16.63}{-15.56}$	$\frac{6.35*10^{14}}{2.17*10^{13}}$	0.19
SVK11-2	'conventional' p.flow	log-normal	bimodal	$\frac{-19.16}{-16.54}$	$\frac{1.43*10^{15}}{3.57*10^{15}}$	0.30
SVK2-8	ash-rich flow	log-normal	unimodal	-15.10	$2.97 * 10^{14}$	0.37
GRC4-11	subplinian fall	log-normal	unimodal	-15.55	$3.03 * 10^{14}$	0.16
GRC4-12	ash-rich flow	log-normal	bimodal	$\frac{-14.62}{-11.88}$	$\frac{3.19*10^{13}}{2.19*10^{12}}$	0.16
GRC1-R	subplinian fall	log-normal	bimodal	$\frac{-17.74}{-15.59}$	$\frac{2.94*10^{14}}{2.42*10^{14}}$	0.33

Table 7: Summary of the study ash samples and their relevant BSD features from SSEM analysis.

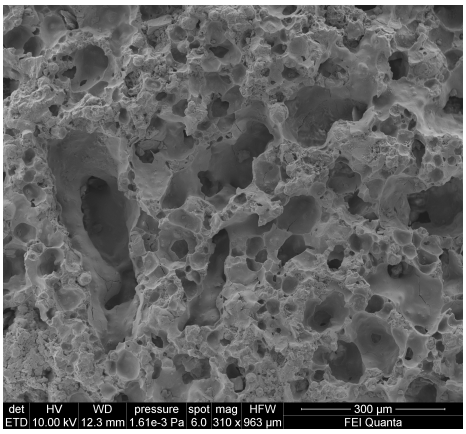

(a) GRC strombolian fall (GRC3-d)

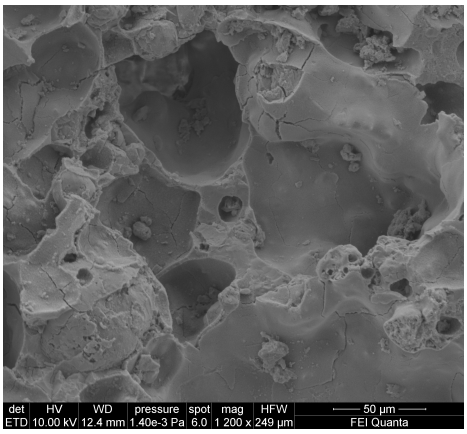

(b) detail of GRC3-d

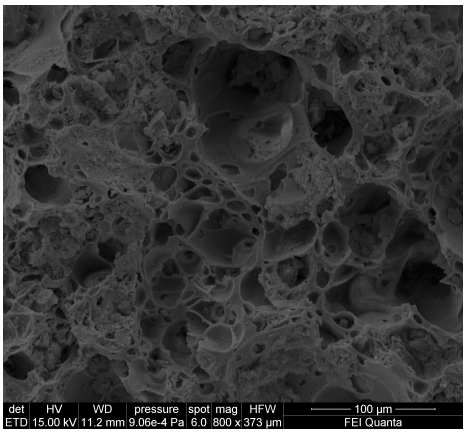

(c) GRC subplinian fall (GRC1-h)

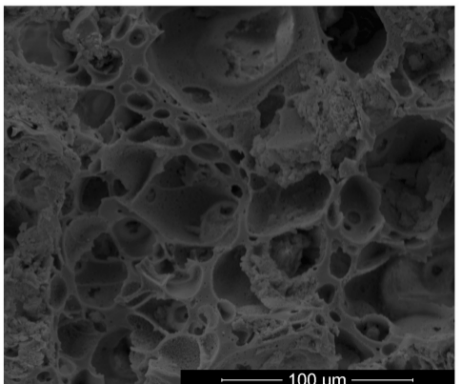

(d) detail of GRC1-h

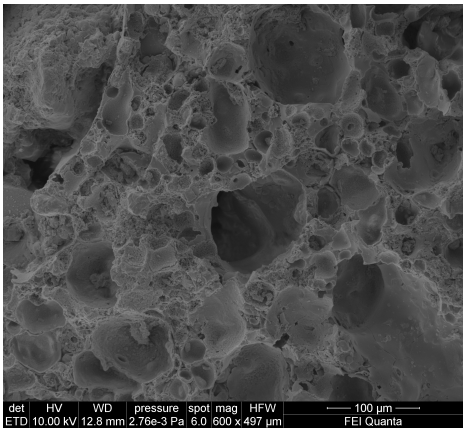

(e) GRC ash-rich flow (GRC4-4)

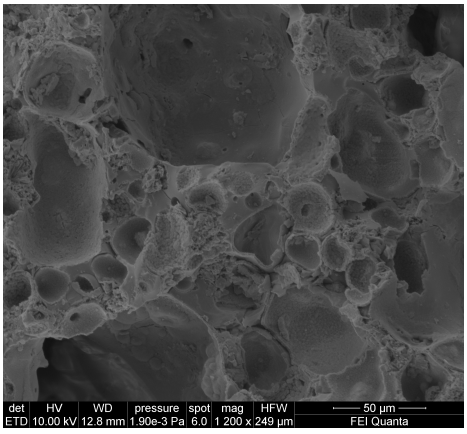

(f) detail of GRC4-4

Figure 17: Texture of lapilli from Grotte di Castro eruption (GRC).

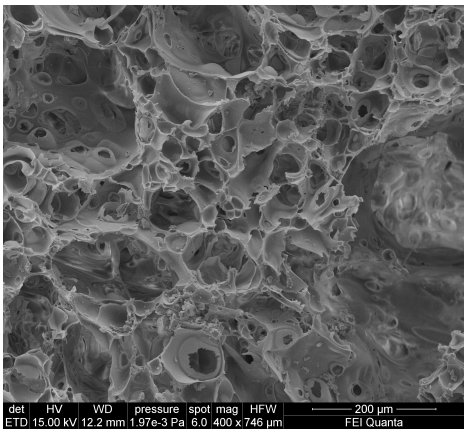

(a) SVK ash-rich flow (SVK2-8)

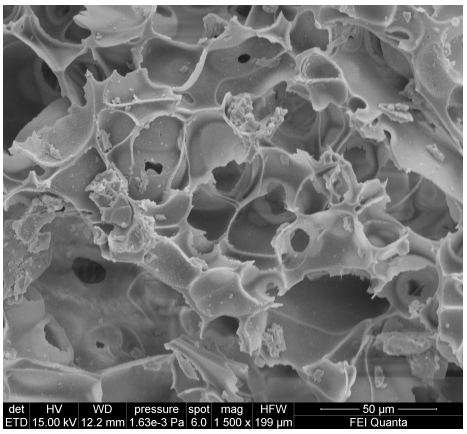

(b) detail of SVK2-8

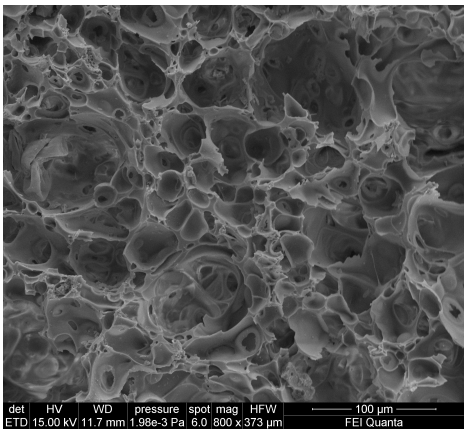

(c) SVK ash-rich flow (SVK11-1)

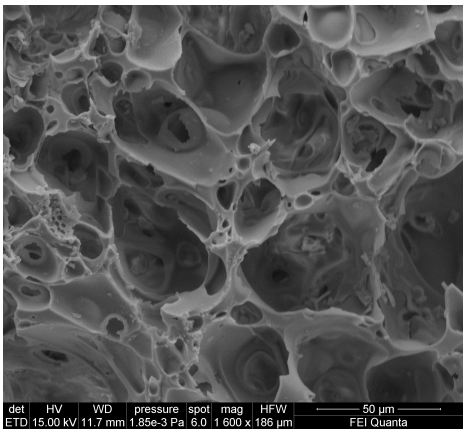

(d) detail of SVK11-1

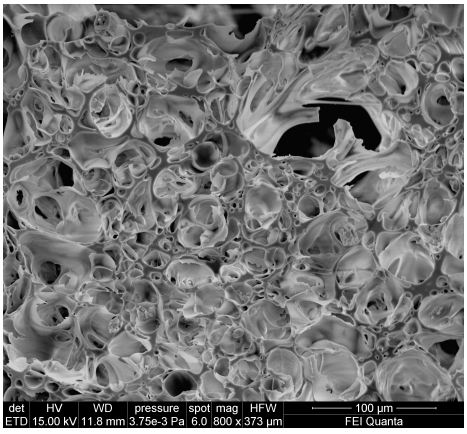

(e) SVK 'conventional' flow (SVK11-2)

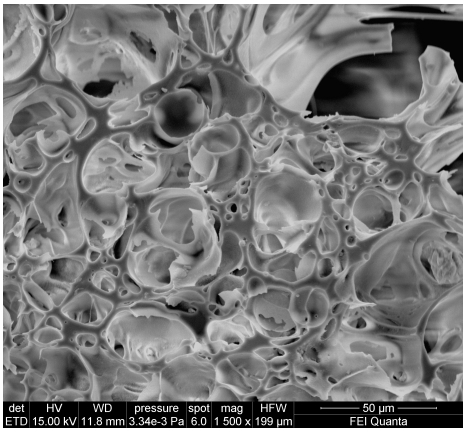

(f) detail of SVK11-2

Figure 18: Texture of juvenile lapilli from Sovana eruption (SVK).

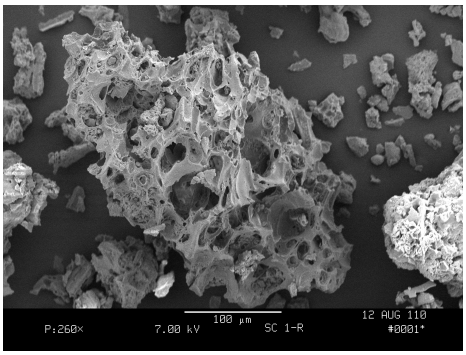

(a) GRC subplinian fall (GRC1R)

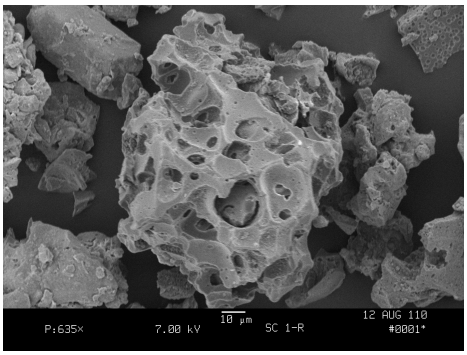

(b)

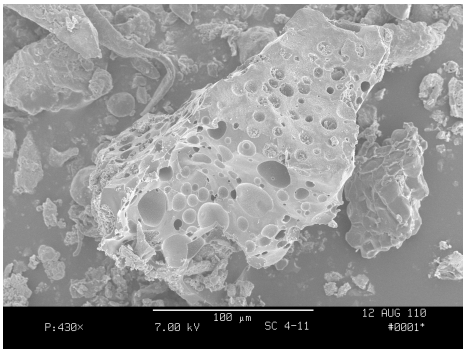

(c) GRC subplinian fall (GRC411)

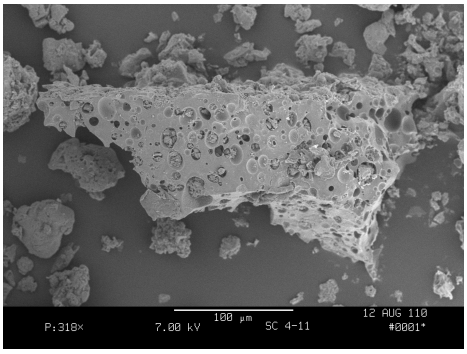

(d)

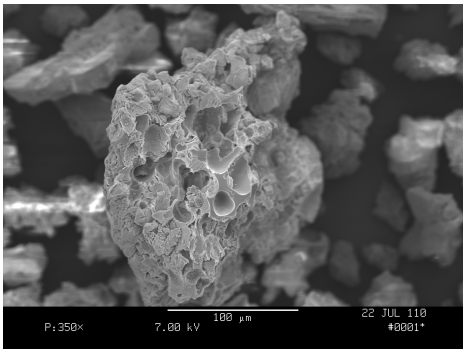

(e) GRC ash-rich flow (GRC4-12)

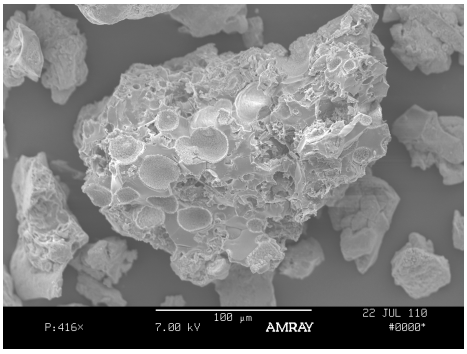

(f)

Figure 19: Ash samples from Grotte di Castro eruption (GRC). The high degree of vesicularity, the delicate-irregular surfaces and the absence of typical magma-water interaction signature rule out hydromagmatic fragmentation features also for the ash-rich flow.

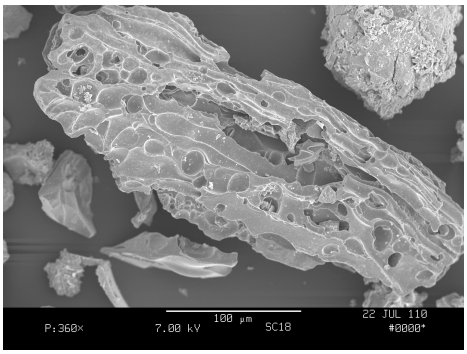

(a) Sovana ash-rich flow (SVK28)

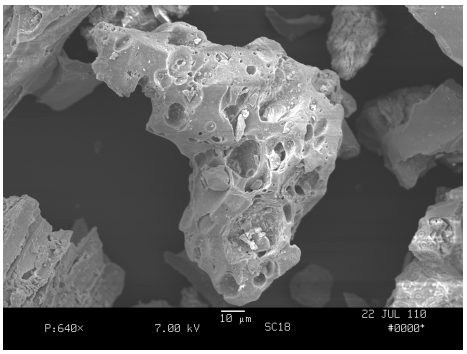

(b)

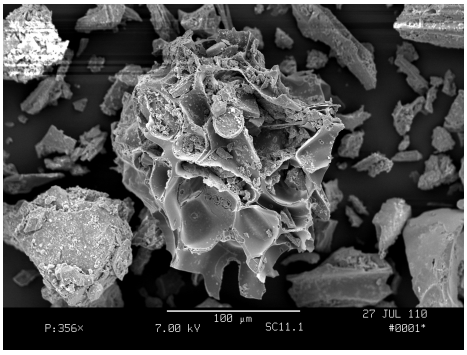

(c) Sovana ash-rich flow (SVK11-1)

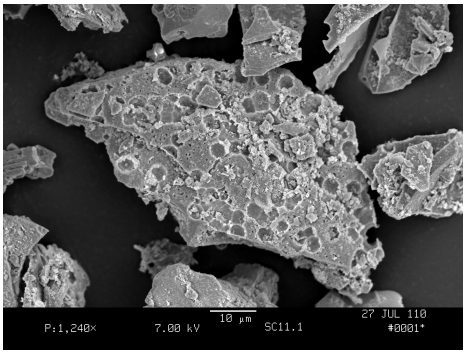

(d)

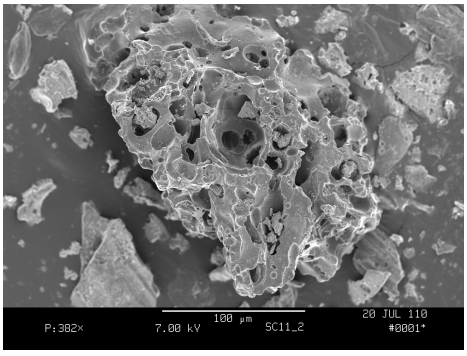

(e) Sovana 'conventional' pyroclastic flow (SVK11-2)

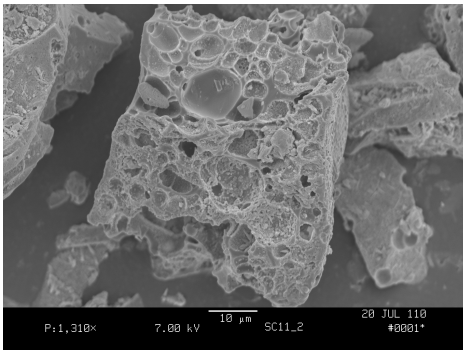

(f)

Figure 20: Ash samples from Sovana eruption (SVK). Also in this case, the absence of typical magma-water interaction features, in both the phases, rules out hydromagmatic fragmentation.

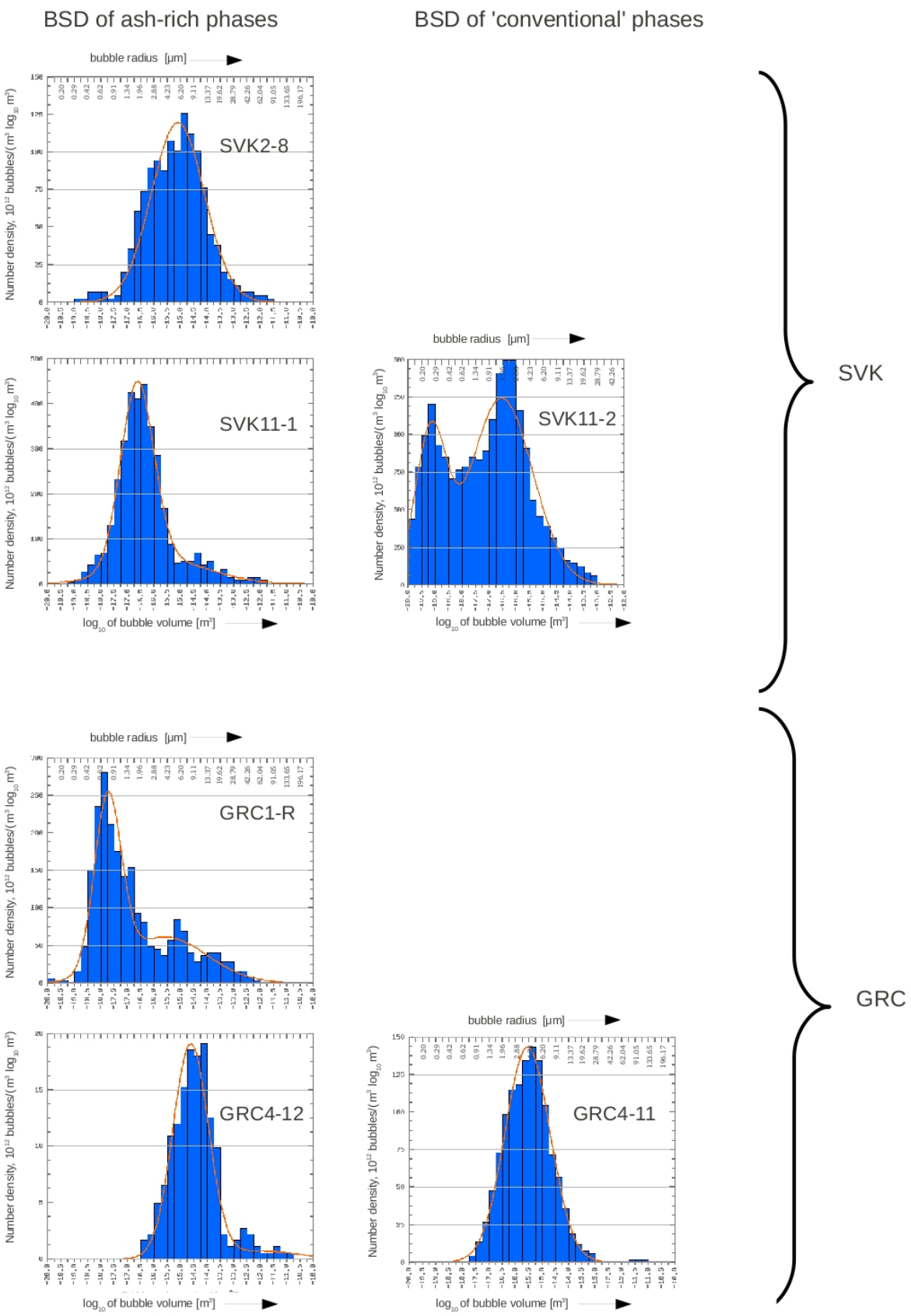

Figure 21: BSD of the studied samples.

6

DISCUSSION

6.1 THE ROLE OF SURFACE TENSION IN BUBBLE NUCLEATION

The gradient theory, successfully applied in several studies of industrial polymers (Poser and Sanchez, 1981; Harrison et al., 1999; Kahl and Enders, 2000; Enders et al., 2005), has been tested here for the first time to numerically model the surface tension of supercritical gas water in contact with trachytic liquid. This method allows to calculate the surface tension, typically evaluated solving the CNT under the heavy assumption of homogeneous nucleation (Fig. 15; Mangan and Sisson, 2005; Gardner and Ketcham, 2011; Gardner, 2012), in a way completely independent from the details of the nucleation process. The surface tension is far to be a constant, but it decreases with increasing nucleation pressure. Experiments (see Fig.16) confirm that surface tension facilitates bubble nucleation at higher pressure. The decompression necessary to nucleate bubbles at high pressure ($> 850 bar$) is at least three times lower than at low pressure ($< 600 bar$)(fig. 16).Instead, the hindered nucleation at relatively low pressure, due to high bubble surface tension, leads to a higher decompression/supersaturation before bubbles nucleate, which may impact the intensity of the eruption enhancing more explosive eruptions (Mangan and Sisson, 2000; Gardner, 2012) at shallow depth ($< 3Km$).

6.2 NUCLEATION AND ASH GENERATION IN THE ASH-RICH ERUPTIONS

The morphoscopic features of juvenile pyroclasts, as well as the paucity of lithic fragments from a possible interacting aquifer, in the study ash-rich deposits rule out a significant hydromagmatic component for the intense magma fragmentation. This work shows that extensive ash production in a dominant magmatic scenario implies high BNDs (ranging from 10^{13} to $10^{15} bubbles/m^3$ in the study cases).

The BND (i.e., the total number of bubbles of all sizes in a m^3 of melt) is not supposed to change as bubbles grow, provided that no new bubbles get nucleated (i.e., magma vesiculation is controlled by a single nucleation event). As bubbles grow, the BSD shifts to the right, i.e. toward increasing bubble sizes. Also, different samples with similar BSD shapes, shifted toward coarser/finer bubbles, indicate increasing/decreasing amounts of bubble growth. By analyzing BSD functions, earlier/deeper bubble nucleation event(s) can be associated with BSD mode(s) toward coarser bubble sizes (i.e., resulting into higher amounts of bubble growth), while later/shallower nucleation event(s) are associated with BSD mode(s) toward finer bubble sizes (i.e., lower amounts of bubble growth).

I suggest that the changing degrees of ash production during the GRC and SVK eruptions is related to changing intra-conduit dynamics, as also recorded

by the observed BSD functions. For each eruption case, the observed modes in the BSD functions reflect more or less complex magma vesiculation history.

The bimodal BSD of the "conventional" pyroclastic flow phase of SVK (SVK11-2; fig.21) thus reflects two major nucleation events of similar intensity (each represented by ca. $10^{15} bubbles/m^3$), producing two distinct bubble subpopulations, respectively centered around $0.3\mu m$ and $2\mu m$ modal sizes. Considering the rapid cooling of fine magma particles upon fragmentation (Proussevitch et al. (2011); I recall that the 125-250 $\mu m - size$ fraction was analyzed on purpose), post-fragmentation bubble nucleation and growth can be assumed negligible. Thus the two nucleation events can be related respectively to a deeper magma vesiculation triggering the explosive eruption and to a later nucleation event occurring during magma ascent in the conduit at shallow depth just prior to fragmentation, as indicated by moderate bubble growth for the finer/earlier bubble subpopulation. The subplinian phase of the GRC eruption (GRC4-11; with magma composition analogous to SVK) is instead characterized by a single dominant nucleation event. The modal bubble size similar to the coarse mode of the previous case, would be consistent with early bubble nucleation occurred at high depth.

The distinctive coarse mode observed in the BSDs of ash-rich phases in both eruption cases indicates that the earlier/deeper nucleation event was quite subordinate in terms of BND (one order of magnitude lower) in comparison to the main nucleation event occurred at shallower depth. The lack of accidental lithics in the ash-rich deposits is consistent with the shallow level of magma fragmentation following the main nucleation event. In the SVK case, the better sorting of BSD of the ash-rich phase vs. the conventional one also testifies an overall less complex vesiculation history of the feeder magma. In the GRC case, where different magma compositions were erupted in the two phases, I cannot exclude the occurrence of two distinct feeder magma batches at different depths.

Also, qualitative SEM analysis of lapilli-sized juvenile clasts (fig. 17, 18) indicates two distinct bubble generations (possibly related to distinct nucleation events) in the GRC ash-rich deposits (fig. 17) and multiple nucleation events in the SVK ash-rich horizon (fig. 18). Different from observation at fine ash-scale, coarser pumice clasts show evidence of ongoing bubble growth and coalescence after fragmentation.

According to the theoretical and experimental results, exposed previously (Fig. 16), lower BND values can be related to hindered nucleation due to high bubble surface tension at relatively low pressure conditions in a shallow magma reservoir. On these grounds, the extensive magma fragmentation during ash-rich eruptive phases, rather than invoking poorly constrained explosive magma-water interaction, can be attributed to the high decompression required to nucleate bubbles in a shallow reservoir. The dominant nucleation event at shallow depth, implying finer BSD, would have led to the collapse of the magmatic foam into an erupting fine-grained gas-pyroclast mixture.

In particular, in the SVK case, the changing degree of fragmentation from the early ash-rich surge to the coarse-grained pyroclastic flow, is possibly related to the changing depth and geometry of magma withdrawal from a common reservoir. An abrupt decompression at the top of the magma body fed the initial

phase of the eruption through a central conduit, whereas a deeper portion of the magma reservoir was involved during the eruption of the pyroclastic flow through the developing ring fractures during ongoing caldera collapse. The overall wider/coarser BSD in the conventional phase would have controlled the overall wider/coarser grain size distribution of the fragmenting magma.

Conversely, the GRC event shows a reverse transition from a "conventional" Subplinian phase to highly fragmented ash-rich surges, concomitant to a substantial shift in the erupted magma composition from phonolite to shoshonite. In this case, we suggest that the high degree of fragmentation of the ash-rich surges is related to the intense decompression of a distinct shoshonitic magma batch located at relatively shallow depth, which was possibly intersected by developing fractures during incipient roof collapse of the phonolitic magma chamber.

In particular, the ash layer heralding the pyroclastic surge activity (GRC1-R), characterised by high bubble nucleation and limited growth, would be consistent with intense decompression at shallow level, while the decreasing bubble nucleation of the succeeding surges (e.g., GRC4-12) would indicate a progressive decay in the decompression rate.

In conclusion, the application of the SSEM technique to determine BSD features of ash particles from Quaternary major explosive eruptions represents a promising approach to gain insights into vesiculation and fragmentation mechanisms leading to peculiar ash-rich eruption phases. The present study provides evidence that extensive ash production was related, rather than to hydromagmatic fragmentation, to the magma decompression history at shallow depth.

7

SUMMARY

The present work addressed the vesiculation process, in particular nucleation, combining numerical modelling, experiments and natural samples analysis. A new approach, based on statistical thermodynamics, allowed the calculation of the magma-water surface tension for a trachytic liquid. The key aspect regards the dependence of surface tension on pressure that affects the bubble nucleation. Nucleation at high pressure (i.e.$>$ 0.8Kbar) is much easier, in terms of decompression/supersaturation. Instead, the hindered nucleation at low pressure (i.e.$<$ 0.8Kbar), due to high bubble surface tension, leads to higher decompression/supersaturation before bubbles nucleate, which may enhance more explosive eruptions (Mangan and Sisson, 2000; Gardner, 2012) at shallow depth ($<$ 3Km).

Decompression experiments have been performed using the HP16/60 Miniclave, an Internally Heated Pressure Vessel that allows fast quench and decompression. Nucleation values obtained by the experiments match well the numerical model.

Natural samples of ash-rich explosive eruptions have been analysed, in terms of nucleation and growth, in order to infer the mechanism of ash formation from the features preserved on the ash particles. The data have been acquired using a novel application of the Stereo Scanning Electron Microscopy (SSEM) that allows 3D measurements of the bubbles. The morphologic features and the lithic-poor nature of the study deposits rule out hydromagmatic fragmentation for ash production. Therefore the extensive ash-production can be related to the high decompression necessary to nucleate bubbles at shallow depth, where the surface tension is higher.

The present work shows that in nature macroscale-processes (e.g., volcanic activity) are strictly controlled by processes acting at the microscale (e.g., bubble nucleation). The Statistical Mechanics is the way to relate microscale and macroscale processes. In the next future, this kind of approach may be applied to crystal phases (e.g., nucleation, dissolution of crystals) and to the interplay of crystals and bubbles, by means of Monte Carlo and Molecular Dynamics simulations.

Part I

APPENDIX

APPENDIX

A.1 CODE

Listing 1: Pure component parameters

```
% This program calculates  pure component parameters rho_pr, P_pr, T_pr
% of the equation of state (EOS) for each component.
% The EOS is based on Sanchez & Lacombe (1976) J. Chem. Phys. Vol. 80, N
    .21, 2352-2362.
% The best fit algorithm uses the MATLAB function fmincon (optimization
    toolbox)
% Simone Colucci, 'Sapienza'- UniversitÃă di Roma, Italy (January 2012)

clear all; close all; clc;
scsz = get(0,'ScreenSize');
%--------------------------------------------------------------------------
%                              EXPERIMENTAL DATA
%--------------------------------------------------------------------------
% The experimental data are reported in
% Lange & Carmichael, Mineralogical Society of America-Reviews in
% Mineralogy, 1990, Vol.24, p.36
Rgas=8.3144621;        % Gas constant [J/(mol*K)]
%.................................MAGMA.................................

%%%%%%%%%%%%%%%%%%%%%%%%%%%% input data
Tmin = 1000 + 273; % [K]
Tmax = 1400 + 273;
T_exp = linspace(Tmin,Tmax,10);
Pmin = 500; % [Bar]
Pmax = 2000;
P_exp = linspace(Pmin,Pmax,10);
% [SiO2,TiO2,Al2O3,Fe2O3,FeO,MgO,CaO,Na2O,K2O,Li2O]
Xi = [0.699,0.002,0.126,0.004,0.023,0.004,0.022,0.068,0.051,0.000]; %[molar
     fraction]
Mi =
    [60.084,79.865,101.961,159.687,71.844,40.304,56.077,61.979,94.195,29.881];
       % molar mass [g/mol]
Vi_1673 = [26.90,23.16,37.11,42.13,13.65,11.45,16.57,28.78,45.84,16.85]; %
    [cm^3/mol]
wt_Vi_1673=[0.06,0.26,0.18,0.28,0.15,0.13,0.09,0.10,0.17,0.15]; % weights
dVi_dT = 1e-3*[0.00,7.24,2.62,9.09,2.92,2.62,2.92,7.41,11.91,5.25]; % [cm
    ^3/K*mol]
wt_dVi_dT=1e-3*[0.50,0.46,0.17,3.49,1.62,0.61,0.58,0.58,0.89,0.81];
dVi_dP = 1e-4*[-1.89,-2.31,-2.26,-2.53,-0.45,0.27,0.34,-2.40,-6.75,-1.02];
    % [cm*3/Bar*mol]
wt_dVi_dP=1e-4*[0.02,0.06,0.09,0.09,0.03,0.07,0.05,0.05,0.14,0.06];
%%%%%%%%%%%%%%%%%%%%%%%%%%%%
for p=1:length(P_exp)
    for t=1:length(T_exp)
```

```
        V_liq(p,t) = sum(Xi.*(Vi_1673 + dVi_dT.*(T_exp(t)-1673) + dVi_dP.*(
            P_exp(p)-1))); % [cm^3/mol]
        wt_V_liq(p,t)=sqrt(sum((Xi.^2).*(wt_Vi_1673.^2 + (wt_dVi_dT.*(T_exp
            (t)-1673)).^2 + (wt_dVi_dP.*(P_exp(p)-1)).^2)));
        rho_exp(p,t) = sum(Xi.*Mi)./V_liq(p,t); %[g/cm^3]
        wt_rho_exp(p,t)=sqrt(sum(((Xi.*Mi).^2)./(wt_V_liq(p,t).^2)));
    end
end
%.....................................................................
disp('------ plot density data of magma component-------');
figure(1)
subplot(1,2,1)
for p=1:length(P_exp)
        plot(T_exp,rho_exp(p,:),'+','MarkerSize',7,'MarkerFaceColor','m','
            MarkerEdgeColor','m')
        hold on
end
axis([1200 1700 1 4]);
xlabel('Temperature (K)')
ylabel('Density (g/cm^3)')
title('Temperature dependence of magma density at various pressures','
    fontsize',16)
subplot(1,2,2)
for t=1:length(T_exp)
        plot(P_exp,rho_exp(:,t),'+','MarkerSize',7,'MarkerFaceColor','m','
            MarkerEdgeColor','m')
        hold on
end
axis([500 2000 1 4]);
xlabel('Pressure (Bar)')
ylabel('Density (g/cm^3)')
title('Pressure dependence of magma density at various temperatures','
    fontsize',16)
box on;
%---------------------------------------------------------------------
%                       PURE COMPONENT PARAMETERS
%---------------------------------------------------------------------

%..................... MAGMA COMPONENT.............................
%%%%%%%%%%%%%%%%%%%%%% Input Data
Mmg= sum(Xi.*Mi)*1e-3 ;              % Molar mass (Kg/mol)
% sigma and mean of gaussian distribution of starting points
sigma_Pi = 20000*1e-1;  % [MPa]
sigma_Ti= 30000;         % [K]
sigma_rhoi= 5*1e3;     % [Kg/m^3]
mean_Pi = 5000*1e-1;
mean_Ti =3000+273;
mean_rhoi =5*1e3;
inflim_P=1;     % solution's range, lower and...
inflim_T=1;
inflim_rho= max(max(rho_exp))+1;
suplim_P=50000*1e-1;    % ... upper boundaries
suplim_T=50000+273;
suplim_rho=10*1e3;
%%%%%%%%%%%%%%%%%%%%%%%%
P_exp=P_exp*1e-1;
```

```
rho_exp=rho_exp*1e3;
P_cs=P_exp(1)*ones(1,length(T_exp));
P_exp1=P_exp;
for i=2:length(P_exp)
    Ap_P=P_exp(i)*ones(1,length(T_exp));
    P_cs=[P_cs Ap_P];
    P_exp1=[P_exp1 P_exp];
end
T_cs=T_exp(1)*ones(1,length(P_exp));
T_exp1=T_exp;
for i=2:length(T_exp)
    Ap_T=T_exp(i)*ones(1,length(P_exp));
    T_cs=[T_cs Ap_T];
    T_exp1=[T_exp1 T_exp];
end
P=[P_exp1 P_cs];
T=[T_cs T_exp1];
rho_P=rho_exp(:,1);
rho_P=rho_P';
rho_T=rho_exp(1,:);
for i=2: length(rho_exp(1,:))
    Ap_rho_P=rho_exp(:,i);
    Ap_rho_P=Ap_rho_P';
    rho_P=[rho_P Ap_rho_P];
    rho_T=[rho_T rho_exp(i,:)];
end
rho_exp1=[rho_P rho_T];
wt_rho_P=wt_rho_exp(:,1);
wt_rho_P=wt_rho_P';
wt_rho_T=wt_rho_exp(1,:);
for i=2: length(wt_rho_exp(1,:))
    Ap_wt_rho_P=wt_rho_exp(:,i);
    Ap_wt_rho_P=Ap_wt_rho_P';
    wt_rho_P=[wt_rho_P Ap_wt_rho_P];
    wt_rho_T=[wt_rho_T wt_rho_exp(i,:)];
end
wt_rho_exp1=[wt_rho_P wt_rho_T];
P=P';T=T';rho_exp1=rho_exp1'; sigma=wt_rho_exp1';
%.....................Call Min Search function.....................
disp('------ START MIN SEARCH MAGMA-------');
[Pmg_pr, Tmg_pr, rhomg_pr]= minsearch(Mmg, P, T,rho_exp1,inflim_P,inflim_T
    ,...
                                      inflim_rho,suplim_P,suplim_T,suplim_
                                          rho,...
                                      sigma_Pi,sigma_Ti,sigma_rhoi,...
                                      mean_Pi,mean_Ti,mean_rhoi,sigma); % [
                                          MPa, K, Kg/m^3]
rmg=((Mmg*Pmg_pr)/(Rgas*Tmg_pr*rhomg_pr))*1e6;
%.....................WATER COMPONENT.............................
% Data from Machida, Sato and Smith,  Fluid Phase Equilibria, 2010,
% Vol. 297, pp. 205-209.
Mw= 18.01528*1e-3;       % Molar mass (Kg/mol)
alpha=1/207;
eps0= 7447;    % [J/mol]
%eps=eps0*(alpha*T/1+alpha*T); % [J/mol]
v= 2.614;   % [cm^3/mol]
```

```
r= 5.823;   % [adim]
%Tw_pr= eps/Rgas;     % [K]
%Pw_pr= eps/v;     % [MPa=J/cm^3]
%rhow_pr= 1e6*Mw*Pw_pr/(Rgas*Tw_pr*r);   % [Kg/m^3]
%------------------------PLOT BEST FIT FUNCTIONS---------------------------
figure(1)
subplot(1,2,1)
for p=1:length(P_exp)
    for t=1:length(T_exp)
        Pmg_rd=P_exp(p)./Pmg_pr;
        Tmg_rd=T_exp(t)./Tmg_pr;
        rhomg_rd=EOS1(Pmg_rd, Tmg_rd,rmg);
        rhomg=rhomg_rd*rhomg_pr;
        rhomg=rhomg*1e-3;
        plot(T_exp(t),rhomg,'o','MarkerSize',4,'Color','k')
        axis([1200 1700 1 4]);
        hold on
    end
end
subplot(1,2,2)
for t=1:length(T_exp)
    for p=1:length(P_exp)
        Pmg_rd=P_exp(p)./Pmg_pr;
        Tmg_rd=T_exp(t)./Tmg_pr;
        rhomg_rd=EOS1(Pmg_rd, Tmg_rd,rmg);
        rhomg=rhomg_rd*rhomg_pr;
        rhomg=rhomg*1e-3;
        P_exp_plot=P_exp(p)*1e1;
        plot(P_exp_plot,rhomg,'o','MarkerSize',4,'Color','k')
        hold on
        axis([500 2000 1 4]);
    end
end
```

```
function h = eos24c(rho_rd,T_rd,P_rd,r)
% EOS (24c), Sanchez and Lacombe (1976)
h = 1 - exp(-rho_rd.^2./T_rd - (1-1./r).*rho_rd - P_rd./T_rd);
```

```
function h1 = EOSroots(rho_rd,T_rd,P_rd,r)
% roots of EOS (24c), Sanchez and Lacombe (1976)
h1 = rho_rd - eos24c(rho_rd,T_rd,P_rd,r);
```

```
function [P_pr T_pr rho_pr]=minsearch(M, P, T,rho_exp,inflim_P,inflim_T,
    inflim_rho,suplim_P,...
                                suplim_T,suplim_rho,sigma_Pi,sigma_Ti,sigma_
                                    rhoi,mean_Pi,mean_Ti,mean_rhoi,sigma)

options = optimset('TolFun',1e-7,'TolX',1e-7,'MaxFunEvals',2000,'MaxIter
    ',2000,'Algorithm','interior-point','Display','off');
for in= 1:100
    disp(in);
    Pi_pr(in)= abs(normrnd(mean_Pi,sigma_Pi));       % fmincon starting
        points
    Ti_pr(in)= abs(normrnd(mean_Ti,sigma_Ti));
    rhoi_pr(in)= abs(normrnd(mean_rhoi,sigma_rhoi));
```

```
[BF,fval,exitflag]= fmincon(@(VAR) X2_EOS(VAR,M, P, T,rho_exp,sigma),...
                        [Pi_pr(in),Ti_pr(in),rhoi_pr(in)],[],[],[],[],...
                        [inflim_P,inflim_T,inflim_rho],[suplim_P,suplim_T,
                            suplim_rho],[],options);
    Pbf(in) = BF(1);
    Tbf(in) = BF(2);
    rhobf(in) = BF(3);
    bf_chi(in) = fval;
    bf_ef(in) = exitflag;
end
[X2v, Ix] = min(bf_chi);
P_pr = Pbf(Ix);
T_pr = Tbf(Ix);
rho_pr = rhobf(Ix);
scsz = get(0,'ScreenSize');
figure('Position',[50 50 0.8*scsz(3) 0.8*scsz(4)],'Name','STATISTICS:
    UPLIFT INVERSION');
iP = linspace(min(Pi_pr),max(Pi_pr),10);
iT = linspace(min(Ti_pr),max(Ti_pr),10);
irho = linspace(min(rhoi_pr),max(rhoi_pr),10);
subplot(2,5,1); hist(bf_ef,20); title(strcat('exitflag: ',sprintf(' %2.0f',
    bf_ef(Ix))));
subplot(2,5,2); hist(bf_chi,5); title(strcat('\chi^2: ',sprintf(' %4.2f',X2
    v)));
subplot(2,5,3); hist(Pi_pr,iP); title('Pressure');
subplot(2,5,4); hist(Ti_pr,iT); title('Temperature');
subplot(2,5,5); hist(rhoi_pr,irho); title('Density');
subplot(2,5,8); hist(Pbf,length(iP)); title(strcat('bf Pressure: ',sprintf
    ('%4.0f',P_pr)));
subplot(2,5,9); hist(Tbf,length(iT)); title(strcat('bf Temperature: ',
    sprintf('%4.0f',T_pr)));
subplot(2,5,10); hist(rhobf,length(irho)); title(strcat('bf Density: ',
    sprintf('%4.0f',rho_pr)));
disp('Pure component parameters-Polymer')
disp('Pressure(MPa) Temperature(K) Density(Kg/m^3)')
disp(P_pr);disp(T_pr); disp( rho_pr);
disp('Chi square per degrees of freedom =')
disp(min(bf_chi))
```

```
function [rad] = EOS1(P_rd_root, T_rd_root,r_root)
% this function calculates the liquid density, representing the root of EOS
% equation with the maximum value
% Sanchez & Lacombe (1976). An Elementary Molecular Theory of Classical
    Fluids
% J. Chem. Phys. Vol. 80, N.21, 2352-2362.

  rho_rd_root = linspace(-0.1,0.99999,100);
  IRoots = sign(EOSroots(rho_rd_root,T_rd_root,P_rd_root,r_root));
  K=0;
  for i=2:length(IRoots)
    flag(i) = IRoots(i) + IRoots(i-1);
    if flag (i) == 0
       K=K+1;
       X0(K,1) = rho_rd_root(i-1);
       X0(K,2) = rho_rd_root(i);
    end;
```

```
  end;
  for k=1:K
      rad(k) = fzero(@(rho_rd_root) EOSroots(rho_rd_root,T_rd_root,P_rd_
          root,r_root), X0(k,:));
  end
  if K==0
      rad=10*1e6;
      disp('rad=0');
  end
  if length(rad)==2 && min(rad)<=0
      disp('there are more than 1 roots => there is a gas phase of
          component 1 or of the binary mixture')
      disp(rad);
      rad=max(rad);
  elseif length(rad)>1 && min(rad)>0
      disp('there are more than 1 roots => there is a gas phase of
          component 1 or of the binary mixture')
      disp(rad);
      rad=10*1e6;
  end
```

```
function X2f=X2_EOS(VAR,M,P, T,rho_exp,sigma)
% chi square per degrees of freedom function for a 3 parameters model

P_pr = VAR(1); T_pr = VAR(2); rho_pr = VAR(3);
R= 8.3144621; % gas constant (J/mol*K)
r = ((M*P_pr)/(R*T_pr*rho_pr))*1e6;
 for j=1:length(P);
    P_rd=P(j)/P_pr;
    T_rd=T(j)/T_pr;
    rho_rd = EOS1(P_rd, T_rd,r); %reduced density of the liquid phase (max
        density)
    rho_rd=max(rho_rd);
    rho(j)=rho_rd*rho_pr;
 end
model = rho;
data = (rho_exp)' ;                    % vector of experimental data
r = data - model ;                     % residual
r=r';
L=length(P);
Wd=diag(1./sigma.^2);
X2 = r'*Wd*r;                          % Chi Square - full covariance
p = length(VAR);                       % number of parameters
N = length(data);                      % number of data points
X2f = X2/(N-p);                        % Chi Square per degrees of freedom
```

Listing 2: Binary parameter

```
% This program calculates  binari interaction parameter k12 of the binary
% mixture magma-water.The mixing rules of the binary EOS are based on
% Lacombe and Sanchez (1976) J. Chem. Phys. Vol. 80, N.23, 2568-2580.
% The best fit algorithm uses the MATLAB function fmincon (optimization
    toolbox)
% Simone Colucci, 'Sapienza'- UniversitÃă di Roma, Italy (January 2012)

clc;
```

```
clear all;close all;
%-------------------------input data-------------------------------------

Rgas=8.3144621;          % gas constant (J/mol*K)
% experimental solubility
Psol=linspace(10,200,10);
Tsol=1273*ones(length(Psol),1); % [K]
Psol1=[69, 69, 69, 69, 103, 103, 103, 103, 103, 207, 207, 207, 207, 207]';
     % [MPa] De Rita et al., 1973
wexp1=1e
    1*[2.45,2.29,2.28,1.21,5.10,3.56,3.29,2.31,3.41,6.85,6.76,6.20,5.59,4.40]';
     %[weight fraction mg/g]
Psol2=[20,40,40,40,50,80,100,100,130,150,150,200,200,200]';% [MPa] Di
    Matteo et al., 2004
wexp2=1e
    1*[0.93,2.77,1.81,1.88,3.22,3.97,5.34,5.21,6.16,6.22,6.38,6.83,5.73,7.43]';
     %[weight fraction mg/g]
Err2=1e
    1*[0.21,0.35,0.11,0.28,0.42,0.25,0.14,0.45,0.34,0.79,0.30,0.55,0.16,0.34];

% Pure component parameters of magma
P_pr=4.9156*1e3;   % (MPa)
T_pr=4.4491*1e3;   % (K)
rho_pr=2.4731*1e3; % (Kg/m^3)
M= 67.7*1e-3;      % magma molecular weight (Kg/mol)
rpol = ((M*P_pr)/(Rgas*T_pr*rho_pr)) *1e6;
% Pure component parameters of water
alpha=1/207;   % [1/K]
eps0= 7447;    % [J/mol]
v= 2.614;      % [cm^3/mol]
rcd= 5.823;    % [adim]
Mcd= 18.01528*1e-3;      % water molecular weight (Kg/mol)
eps=eps0*(alpha*Tsol(1)./(1+alpha*Tsol(1))); % [J/mol]
Tcd_pr= eps/Rgas;     % [K]
Pcd_pr= eps/v;        % [MPa=J/cm^3]
rhocd_pr= 1e6*Mcd*Pcd_pr./(Rgas*Tcd_pr.*rcd);
k12=-0.0355;  % unknown
%----------------------plot experimental data ----------------------------
disp('------ plot solubility data -----------');
figure(1)
plot(Psol1,wexp1*1e-3,'ok');
axis([0 210 0 0.1])
hold on
errorbar(Psol2,wexp2*1e-3,Err2*1e-3,'xk');
axis([0 210 0 0.1])
hold on
% --------------------minsearch solubility--------------------------------
disp('------ START MIN SEARCH SOLUBILITY-------');
inflim_k12 = -20;
suplim_k12 =  5;
mean_k12i =  -10;
sigma_k12i =  10;
phi1=solubility( k12,Tsol,Psol, P_pr, Pcd_pr, Tcd_pr,T_pr,rhocd_pr,rho_pr,
    Rgas,rcd,rpol,Mcd,M);
w_cd = (phi1.*rhocd_pr)./(rho_pr-(phi1.*rho_pr) + (phi1.*rhocd_pr));
%-------------------------Densities -------------------------------------
```

```
P_rd=Psol./P_pr;
T_rd=Tsol./T_pr;
Pcd_rd=Psol./Pcd_pr;
Tcd_rd=Tsol./Tcd_pr;
 for k=1:length(Psol)
   % Reduced Densities
    [rho_bin_rd(k),rho_bin_pr(k),Not3] = mix_rules(Psol(k),Tsol(k),phi1(k),
        Pcd_pr,P_pr,Tcd_pr,T_pr, rhocd_pr,rho_pr,rcd,rpol,Mcd,M,k12);
    rho_rd(k) = EOS1_anew(P_rd(k), T_rd(k),rpol);
    rhocd_rd(k) =  EOS1_anew(Pcd_rd(k), Tcd_rd(k),rcd);
   % Densities of pure components and binary mixture
    rho_bin(k) = rho_bin_rd(k)*rho_bin_pr(k);
    rho(k) = rho_rd(k)*rho_pr;
    rhocd(k) = rhocd_rd(k)*rhocd_pr;
end
%-----------------------plot model----------------------------------------
figure(2)
plot(Psol,rho,'-k');
hold on
xlabel('P(MPa)')
ylabel('magma density (Kg/m^3)')
title('Density of hanydrous magma ','fontsize',16)
box on;
figure(3)
plot(Psol,rhocd,'-k');
hold on
xlabel('P(MPa)')
ylabel('water density (Kg/m^3)')
title('Density of water ','fontsize',16)
box on;
figure(4)
plot(Psol,rho_bin,'-k');
hold on
xlabel('P(MPa)')
ylabel('magma density (Kg/m^3)')
title('Density of magma+water ','fontsize',16)
box on;
figure(1)
plot(Psol,w_cd,'-k','MarkerSize',7,'MarkerFaceColor','y','MarkerEdgeColor
    ','r');
hold on
xlabel('Pressure (MPa)')
ylabel('weight fraction (g_{gas}/g_{pol})')
%title('Solubility of Carbon Dioxide in SA','fontsize',16)
axis([0 210 0 0.1]);
box on;
```

```
function [mi ] = chem_pot_bin( R,phi_root,r1,r2,phi2,r1_0,rho_bin_par,rho_
    bin,P1_pr,P2_pr,Pmatr,T1_rd,T,P1_rd )
%this function calculates the chemical potential of the binary mixture

mi = R*T.*(log(phi_root) + (1-r1/r2).*phi2 + r1_0*rho_bin_par.*...
    ((P1_pr+P2_pr-2*Pmatr(1,2))./(P1_pr.*T1_rd)).*phi2.^2) + ...
      r1_0*R*T.*(-rho_bin_par./T1_rd + P1_rd./(rho_bin.*T1_rd) ...
      + (1./rho_bin).*(( 1 - rho_bin_par).*log(1-rho_bin_par) + (rho_bin_
          par/r1_0).*log(rho_bin_par)));
```

```
end
```

```
function h = eos24cnew(rho_rd,T_rd,P_rd,r)

h = 1 - exp(-rho_rd.^2./T_rd - (1-1./r).*rho_rd - P_rd./T_rd);
```

```
function [rad] = EOS1_anewbin(P_rd, T_rd,r)
% Reference
    ********************************************************************************

% Sanchez & Lacombe (1976). An Elementary Molecular Theory of Classical
    Fluids
% J. Chem. Phys. Vol. 80, N.21, 2352-2362.
%
    ********************************************************************************


rho_cryt2=5;
rho_cryt1=-1;
r_aux=1-1/r;
discr=4+(T_rd*r_aux)^2 -4*T_rd*r_aux-8*T_rd/r;
if discr>0
    rho_cryt2=-0.25*(T_rd*r_aux -2 -sqrt(discr));
    rho_cryt1=-0.25*(T_rd*r_aux -2 +sqrt(discr));
end
F_cryt1=-rho_cryt1 + 1 - exp(-rho_cryt1.^2./T_rd - (1-1./r).*rho_cryt1 - P_
    rd./T_rd);
F_cryt2=-rho_cryt2 + 1 - exp(-rho_cryt2.^2./T_rd - (1-1./r).*rho_cryt2 - P_
    rd./T_rd);
if rho_cryt1>0 && rho_cryt2<5 && (F_cryt2*F_cryt1)<0
    if 0>=F_cryt1>=-0.1 && (F_cryt2*F_cryt1)<0
        rho_aux = linspace(0,5,1000);
        F_aux=-rho_aux + 1 - exp(-rho_aux.^2./T_rd - (1-1./r).*rho_aux - P_
            rd./T_rd);
        IRoots = sign(F_aux);
        K=0;
        for i=2:length(IRoots)
            flag(i) = IRoots(i) + IRoots(i-1);
            if flag (i) == 0
                K=K+1;
                X0(K,1) = rho_aux(i-1);
                X0(K,2) = rho_aux(i);
            end
        end
        for k=1:K
            rad(k)= fzero(@(rho_rd) eosrootsnew(rho_rd,T_rd,P_rd,r), X0(k
                ,:));
        end
        rad=max(rad);
    else
        rad=10;
        disp('too much roots! rad=10');
        pause
    end
else
```

```
    rad= fzero(@(rho_rd) eosrootsnew(rho_rd,T_rd,P_rd,r), [0,5]);
end
```

```
function h=equilibrium_bin(phi_root,T,P,P1_pr,P2_pr,T1_pr,T2_pr,rho1_pr,rho
    2_pr,T1_rd,P1_rd,r1_0,r2_0,R,M1,M2,k12)

rho1 = EOS1_anew(P1_rd, T1_rd,r1_0);
mi1 = chem_potnew(T,rho1,P1_rd,T1_rd,r1_0); % chemical potential of 1 in
    the gas phase, it is equivalent to the pure
                                            % chem. pot. because only
                                                component 1 is present in
                                                the gas phase
for k=1:length(phi_root)
    phi2(k)=1-phi_root(k);
    [rho_bin_rd(k),rho_bin_pr(k),Pmatr]=mix_rules(P,T,phi_root(k),P1_pr,P2_
        pr,T1_pr,T2_pr, rho1_pr,rho2_pr,r1_0,r2_0,M1,M2,k12);
end
rho_bin_par= rho_bin_rd; %.*phi_root;
mi1_binmix = chem_pot_bin(R,phi_root,r1_0,r2_0,phi2,r1_0,rho_bin_par,rho_
    bin_rd,P1_pr,P2_pr,Pmatr,T1_rd,T,P1_rd);
h = mi1_binmix-mi1;
```

```
function k12=minsearchsol(inflim_k12,suplim_k12,mean_k12i,sigma_k12i,Tsol,
    Psol, wexp,P_pr, P1_pr, T1_pr,T_pr,rho1_pr,rho_pr,R,r1,r,M1,M)

options = optimset('TolFun',1e-7,'TolX',1e-7,'MaxFunEvals',2000,'MaxIter
    ',2000,'Algorithm','interior-point','Display','off');
for in= 1:10
    disp(in);
    k12i(in)= abs(normrnd(mean_k12i,sigma_k12i));       % fmincon starting
        point
[BF,fval,exitflag]= fmincon(@(VAR) X2_sol(VAR,Tsol,Psol, wexp,P_pr, P1_pr,
    T1_pr,T_pr,rho1_pr,rho_pr,R,r1,r,M1,M),...
                        k12i(in),[],[],[],[],...
                        inflim_k12,suplim_k12,[],options);
    k12bf(in) = BF;
    bf_chi(in) = fval;
    bf_ef(in) = exitflag;
end;
[X2v, Ix] = min(bf_chi);
k12 = k12bf(Ix);
scsz = get(0,'ScreenSize');
figure('Position',[50 50 0.8*scsz(3) 0.8*scsz(4)],'Name','STATISTICS:
    UPLIFT INVERSION');
ik = linspace(min(k12i),max(k12i),10);
subplot(2,5,1); hist(bf_ef,20); title(strcat('exitflag: ',sprintf(' %2.0f',
    bf_ef(Ix))));
subplot(2,5,2); hist(bf_chi,5); title(strcat('\chi^2: ',sprintf(' %4.2f',X2
    v)));
subplot(2,5,3); hist(k12i,ik); title('binary parameter');
subplot(2,5,8); hist(k12bf,length(ik)); title(strcat('bf binary parameter:
    ',sprintf('%4.0f',P_pr)));
disp('binary parameter')
disp(k12);
disp('Chi square per degrees of freedom =')
```

```
disp(min(bf_chi))
```

```
function [rad] = root_bin( R,T,P,r1,r2,P1_pr,P2_pr,T1_pr,T2_pr,rho1_pr,rho
    2_pr,M1,M2,k12)

P1_rd=P./P1_pr;
T1_rd=T./T1_pr;
phi_root = linspace(0.00001,0.2,100);
IRoots = sign(equilibrium_bin(phi_root,T,P,P1_pr,P2_pr,T1_pr,T2_pr,rho1_pr,
    rho2_pr,T1_rd,P1_rd,r1,r2,R,M1,M2,k12));
K=0;
for i=2:length(IRoots)
    flag(i) = IRoots(i) + IRoots(i-1);
    if flag (i) == 0
        K=K+1;
        X0(K,1) = phi_root(i-1);
        X0(K,2) = phi_root(i);
    end
end
if K==0
    rad=2;
else
    for k=1:K                                          % find roots
        rad_temp(k) = fzero(@(phi_root) equilibrium_bin(phi_root,T,P,P1_pr,
            P2_pr,T1_pr,T2_pr,rho1_pr,rho2_pr,T1_rd,P1_rd,r1,r2,R,M1,M2,k
            12), X0(k,:));
        if K>1
            phiA= rad_temp(k);
            [rho_test_rd,rho_bin_pr,Not3] = mix_rules(P,T,phiA,P1_pr,P2_pr,
                T1_pr,T2_pr, rho1_pr,rho2_pr,r1,r2,M1,M2,k12);
            rho_test(k) = rho_test_rd*rho_bin_pr;
        end
    end
    rad=rad_temp(1);
    if K>1
        [rho_test_min,ind] = min(rho_test(1:K));
        rad=rad_temp(ind);
        disp('K>1');
    end
end
```

```
function X2f=X2_sol(VAR,Tsol,Psol, wexp,P_pr, P1_pr, T1_pr,T_pr,rho1_pr,rho
    _pr,R,r1,r,M1,M)
% chi square per degrees of freedom function for a 1 parameter model

k12 = VAR;
phi1=solubility( k12,Tsol,Psol, P_pr, P1_pr, T1_pr,T_pr,rho1_pr,rho_pr,R,r
    1,r,M1,M);
w_cd = (phi1.*rho1_pr)./(rho_pr-phi1.*rho_pr+phi1.*rho1_pr);
model = w_cd ;
data = wexp' ;  % vector of experimental data
res = data - model ;% residual
res=res';
L=length(Psol);
sigma=ones(L,1);
```

```
Wd=diag(1./sigma.^2);
X2 = res'*Wd*res;  % Chi Square - full covariance
p = length(VAR);  % number of parameters
N = length(data); % number of data points
X2f = X2/(N-p); % Chi Square per degrees of freedom
```

```
function  mi= chem_potnew(T,rho_rd,P_rd,T_rd,r)

R=8.3144621; % gas constant
mi=r*R*T*(-(rho_rd/T_rd) + (P_rd/(rho_rd*T_rd)) +(1-rho_rd)*log(1-rho_rd)/
    rho_rd + (1/r)*log(rho_rd));
```

```
function [rad] = EOS1_anew(P_rd_root, T_rd_root,r_root)
% this function calculates the liquid density, representing the root of EOS
% equation with the maximum value
% Reference
    ********************************************************************************

% Sanchez & Lacombe (1976). An Elementary Molecular Theory of Classical
    Fluids
% J. Chem. Phys. Vol. 80, N.21, 2352-2362.
%
    ************************************************************************************


  rho_rd_root = linspace(-0.1,0.99999,100);
  IRoots = sign(eosrootsnew(rho_rd_root,T_rd_root,P_rd_root,r_root));
  K=0;
  for i=2:length(IRoots) % find intervals where function changes sign
    flag(i) = IRoots(i) + IRoots(i-1);
    if flag (i) == 0
       K=K+1;
       X0(K,1) = rho_rd_root(i-1);
       X0(K,2) = rho_rd_root(i);
    end
  end
  for k=1:K  % find roots
      rad(k) = fzero(@(rho_rd_root) eosrootsnew(rho_rd_root,T_rd_root,P_rd_
          root,r_root), X0(k,:));
  end
  end
```

```
function h1 = eosrootsnew(rho_rd,T_rd,P_rd,r)
% roots of EOS (24c), Sanchez and Lacombe (1976)
h1 = rho_rd - eos24cnew(rho_rd,T_rd,P_rd,r);
```

```
function [rho_rd,rhobin_pr,Pmatr] = mix_rules(P,T,phiA,P1_pr,P2_pr,T1_pr,T
    2_pr, rho1_pr,rho2_pr,r1,r2,M1,M2,k12)
% Mixing rules for binary mixture (Lacombe Sanchez, 1976, Sato et al.,
    1996)

            Rgas=8.3144621;          % gas constant (J/mol*K)
            P12=(1-k12)*sqrt(P1_pr*P2_pr); % eq.8 (Sato et al., 1996);
                modified from eq.79 (Lacombe Sanchez, 1976)
            P21=P12;
```

```
            P11=P1_pr;
            P22=P2_pr;
            Pmatr=[P11,P12;P21,P22];
            P2_rd = P./P2_pr;
            T2_rd= T./T2_pr;
            phiB=1-phiA;
            phi=[phiA,phiB]; % phi vector eq. 12
            Pbin_pr= ((phiA*phiA*P11)+(phiA*phiB*P12))  + ((phiB*phiA*P21)
                +(phiB*phiB*P22)); % eq.7
            Pbin_rd=P./Pbin_pr;
            phiA_0=(phiA.*P1_pr./T1_pr)./((phiA.*P1_pr./T1_pr)+(phiB.*P2_pr
                ./T2_pr));
            phiB_0=(phiB.*P2_pr./T2_pr)./((phiA.*P1_pr./T1_pr)+(phiB.*P2_pr
                ./T2_pr));
            phi_0=[phiA_0,phiB_0];   % phi_0 vector eq.11
            Tbin_pr=Pbin_pr*(phiA_0*T1_pr/P1_pr + phiB_0*T2_pr/P2_pr);  %
                eq.9
            Tbin_rd=T./Tbin_pr;
            r1_0 = r1;
            r2_0 = r2;
            A=(phiA_0/r1_0)+(phiB_0/r2_0);
            rbin=1./A;
            w1= (phiA.*rho1_pr)./(rho2_pr-(phiA.*rho2_pr) + (phiA.*rho1_pr)
                ); % weight fraction
            w2= (phiB.*rho2_pr)./(rho1_pr-(phiB.*rho1_pr) + (phiB.*rho2_pr)
                );
            v1=Rgas*T1_pr/P1_pr;
            v2=Rgas*T2_pr/P2_pr;
            v1_aux=v1*rho1_pr;
            v2_aux=v2*rho2_pr;
            x1=(w1/v1_aux)/(w1/v1_aux + w2/v2_aux);  % molar fraction
            x2=(w2/v2_aux)/(w1/v1_aux + w2/v2_aux);
            rhobin_pr=1e6*(M2*x2+M1*x1)*Pbin_pr/(Rgas*Tbin_pr*rbin);% eq.
                10
            rho_rd = EOS1_anewbin(Pbin_rd, Tbin_rd,rbin);
end
```

```
function phi1 = solubility( k12,T,P, P2_pr, P1_pr, T1_pr,T2_pr,rho1_pr,rho
    2_pr,R,r1,r2,M1,M2)

% 1=water
phi1=zeros(1,length(P));
for i=1:length(P)
    phi1(i)= root_bin(R,T(i),P(i),r1,r2,P1_pr,P2_pr,T1_pr,T2_pr,rho1_pr,rho
        2_pr,M1,M2,k12);
end
end
```

Listing 3: Surface tension of pure components

```
%  WATER SURFACE TENSION
% This program calculates the surface tension of water.
% Equations from Poser C.I. and Sanchez I.C.(1979). Surface tension theory
% of pure liquids and polymer melts. Journal of Colloid and Interface
% Science, Vol.69, No.3, 539-548.
% Experimental data from Kahl H.and Enders S.(2000). Calculations of
```

```
% surface properties of pure fluids using density gradient theory and
% SAFT-EOS. Fluid Phase equilibria, 172, 27-42.

clear all; close all; clc;
disp('------ plot water surface tension data -----------');
filepath = 'data/water_surface_tension.txt';
[T,st] = textread (filepath, '%f %f' );
figure(1)
plot(T,st,'^','MarkerSize',7,'MarkerFaceColor','y','MarkerEdgeColor','y')
hold on
xlabel('T(K)')
ylabel('surface tension (mN/m)')
title('Surface tension of water','fontsize',16)
box on;
% ------------------------------------------------------------------------
Rgas=8.3144621;          % gas constant (J/mol*K)
alpha=1/207;   % [1/K]
eps0= 7447;    % [J/mol]
v= 2.614;      % [cm^3/mol]
r= 5.823;    % [adim]
M= 18.01528*1e-3;      % water molecular weight (Kg/mol)
eps=eps0*(alpha*T)./(1+(alpha*T)); % [J/mol]
T_pr= eps/Rgas;     % [K]
P_pr= eps/v;        % [MPa=J/cm^3]
rho_pr= 1e6*M*P_pr./(Rgas*T_pr.*r);
k_rd= 0.91;
intg =integral(T,T_pr,r);
st=surf_ten_MB( k_rd,T_pr,P_pr,intg);
figure(1)
plot(T,st,'--','MarkerSize',7,'MarkerFaceColor','y','MarkerEdgeColor','y');
xlabel('T(K)')
ylabel('reduced surface tension (mN/m)')
title('Surface tension of water','fontsize',16)
box on;
axis([200 700 0 90]);
hold on
```

```
function  mi= chem_pot(rho,P,T,r)

v=1./rho;
mi=-rho+P.*v + T.*((v-1).*log(1-rho)+(1/r)*log(rho));
```

```
function h = eos24cnew(rho_rd,T_rd,P_rd,r)
% EOS (24c), Sanchez and Lacombe (1976)

h = 1 - exp(-rho_rd.^2./T_rd - (1-1./r).*rho_rd - P_rd./T_rd);
```

```
function [rad] = EOS1_anew(P_rd_root, T_rd_root,r_root)
% this function calculates the liquid density, representing the root of EOS
% equation with the maximum value
% Reference
    ************************************************************************

% Sanchez & Lacombe (1976). An Elementary Molecular Theory of Classical
    Fluids
```

```
% J. Chem. Phys. Vol. 80, N.21, 2352-2362.
%
    ********************************************************************************

rho_rd_root = linspace(-0.1,0.99999,100);
IRoots = sign(eosrootsnew(rho_rd_root,T_rd_root,P_rd_root,r_root));
K=0;
for i=2:length(IRoots)
    flag(i) = IRoots(i) + IRoots(i-1);
    if flag (i) == 0
        K=K+1;
        X0(K,1) = rho_rd_root(i-1);
        X0(K,2) = rho_rd_root(i);
    end;
end;
for k=1:K
    rad(k) = fzero(@(rho_rd_root) eosrootsnew(rho_rd_root,T_rd_root,P_rd_
        root,r_root), X0(k,:));
end
```

```
function [rad] = EOS1_anew_B(P_rd_root, T_rd_root,r_root)
% this function calculates the liquid density, representing the root of EOS
% equation with the maximum value
% Reference
    ************************************************************************

% Sanchez & Lacombe (1976). An Elementary Molecular Theory of Classical
    Fluids
% J. Chem. Phys. Vol. 80, N.21, 2352-2362.
%
    ********************************************************************************


  rho_rd_root = linspace(-0.00001,1,1000);
  IRoots = sign(eosrootsnew(rho_rd_root,T_rd_root,P_rd_root,r_root));
  K=0;
  for i=2:length(IRoots)
    flag(i) = IRoots(i) + IRoots(i-1);
    if flag (i) == 0
       K=K+1;
       X0(K,1) = rho_rd_root(i-1);
       X0(K,2) = rho_rd_root(i);
    end;
  end;
  for k=1:K
      rad(k) = fzero(@(rho_rd_root) eosrootsnew(rho_rd_root,T_rd_root,P_rd_
          root,r_root), X0(k,:));
  end
  end
```

```
function h1 = eosrootsnew(rho_rd,T_rd,P_rd,r)
% roots of EOS (24c), Sanchez and Lacombe (1976)

h1 = rho_rd - eos24cnew(rho_rd,T_rd,P_rd,r);
```

```
function h= eqroots(P,T,r)

for i=1:length(P);
       rho=EOS1_anew(P(i), T,r);
        rhol(i)=max(rho);
        rhog(i)=min(rho);
end
h=chem_pot(rhol,P,T,r) - chem_pot(rhog,P,T,r) ;
```

```
function  [P_eq]=eq_search(T,r)

P=linspace(0,0.1,100);  %P = linspace(-0.1,0.001,1000)
index2=0;
index1=0;
for j=1:length(P)
    rho=EOS1_anew(P(j), T,r);
    if (length(rho)>1)                % if you are under critical point
        find the roots
        index2=[index2 j];
    elseif (length(rho)==1)
        index1=[index1 j];
    else
        disp('no solutions found')
    end
end
if (length(index2)>1);
    P_coexist=P(index2(2:end));
    maxP=max(P_coexist);
    P2=linspace(0,maxP,100);
    IRoots = sign(eqroots(P2,T,r));
    K=0;
    for l=2:length(IRoots)
        flag(l) = IRoots(l) + IRoots(l-1);
        if flag (l) == 0
            K=K+1;
            X0(K,1) = P2(l-1);
            X0(K,2) = P2(l);
        end
    end
    P_ind=0;
    for i=1:length(IRoots)
        if IRoots(i)==0
            P_ind=[P_ind i];
        end
    end
    if (K==0)
        P_eq=100;
        disp('K=0');
    else
        for k=1:K
            P_eq(k) = fzero(@(P2) eqroots(P2,T,r), X0(k,:));
        end
    end
else
    P_eq=100;
```

```
end
```

```
function [ P_eq rhol rhog] = equilibrium_new(T,r)
% this function calculates the equibrium pressure and densities applying
% the equilibrium criterion based on equaling chemical potentials

A=eq_search(T,r);
if (A==100)
    rhol=30000;
    rhog=10000;
    P_eq=100;
else
    P_eq=A
    if length(P_eq>1)
        P_eq=max(P_eq)
    end
    rho=EOS1_anew_B(P_eq, T,r);
    rhol=max(rho);
    rhog=min(rho);
end
```

```
function [int ] = integral(T,T_pr,r )
%This function calculates the integral of surface tension using trapezoidal
     numerical integration trapz

T_rd=T./T_pr;
for j=1:length(T_rd)
    [ P_eq,rhol,rhog ] = equilibrium_new(T_rd(j),r);
    X=(rhog+((rhol-rhog)/100)):(rhol-rhog)/100:(rhol-((rhol-rhog)/100));
    mi_eq= chem_pot(rhol,P_eq,T_rd(j),r);
    A=X.*mi_eq;
    Y1=P_eq-(X.^2)+T_rd(j).*((1-X).*log(1-X)+(X./r).*log(X));
    Y2=Y1-A;
    Y=Y2.^(1/2);
    disp('mi_eq');disp(mi_eq);
    int(j)=trapz(X,Y);
end
```

```
function [st] = surf_ten_MB( k,T_pr,P_pr,intg)
%this function calculates the surface tension of a pure component

st_rd=(2*(k^(1/2))*intg)'
kBolt=1.38*1e-23;  % Boltzmann constant(J/(K*mol))
P_pr=P_pr*1e6
st_pr=((T_pr.*kBolt).^(1/3)).*((P_pr).^(2/3))  % T=[K];P=[N/m^2];st_pr=[N/m
    ]
st=st_rd.*st_pr*1e3;  %st=[mN/m]
```

Listing 4: Surface tension of the binay mixture

```
% This program calculates  the surface tension of a binary mixture.
% The set of equations is based on
% Poser and Sanchez (1981) Macromolecules, 14, 361-370.
% The integration algorithm uses the MATLAB function quad
% Simone Colucci, 'Sapienza'- UniversitÃă di Roma, Italy (January 2012)
```

```
clear all;close all;clc;
k =1.3806505*1e-23;    % Boltzmann constant [J/K]
Rgas=8.3144621;        % Gas constant [J/(mol*K)]
conv = 4.186*1e3;      % Conversion J-kcal
% equilibrium variables
P_eq = linspace(10,200,10); % [MPa]
T = 1273*ones(1,length(P_eq)); % [K]
% pure components parameters
T2_pr = 4.4491*1e3;   % [K]                      magma
P2_pr = 4.9156*1e3;   % [MPa]
rho2_pr = 2.4731*1e3; % [Kg/m^3]
M2 = 67.7*1e-3;       % molecular weight (Kg/mol)
eps22 = T2_pr*Rgas/conv;          % [kcal/mol]
v2_pr = T2_pr*Rgas/P2_pr;              % [cm^3/mol]
r2 = (1e6)*M2*P2_pr/(Rgas*T2_pr*rho2_pr);    % [adim]
alpha=1/207;   % [1/K]                           water
eps0= 7447;    % [J/mol]
M1= 18.01528*1e-3;      % water molecular weight (Kg/mol)
eps11=eps0*alpha*T./( (1+alpha*T)*conv); % [kcal/mol]
v1_pr= 2.614;      % [cm^3/mol]
r1= 5.823;      % [adim]
T1_pr= eps11*conv./Rgas;     % [K]
P1_pr= eps11*conv./v1_pr;        % [MPa=J/cm^3]
rho1_pr= 1e6*M1*P1_pr./(Rgas*T1_pr*r1);  % [Kg/m^3]
% binary mixture parameters
k12 = -0.0355;   % [adim] % Mixing rules Lacombe and Sanchez, 1976
% interaction parameters
k11_rd = 0.3    ;  %  [adim]
k22_rd = 0.91   ;  %  [adim]
phi1_v = 1;
mi1_eq=zeros(1,length(P_eq));
mi2_eq=zeros(1,length(P_eq));
surf_ten=zeros(1,length(P_eq));
for i=1:length(P_eq)
    % equilibrium chemical potentials
    phi1 = solubility( k12,T(i),P_eq(i), P2_pr, P1_pr(i), T1_pr(i),...
        T2_pr,rho1_pr(i),rho2_pr,Rgas,r1,r2,M1,M2);
    P1_rd=P_eq(i)./P1_pr(i);
    T1_rd=T(i)./T1_pr(i);
    rho1_rd = EOS1_anew(P1_rd, T1_rd,r1);
    mi1_eq(i) = chem_potnew(T(i),rho1_rd,P1_rd,T1_rd,r1);
    mi2_eq(i) = equilibrium_mu((1-phi1),T(i),P_eq(i),P1_rd,T1_rd,P2_pr,P1_
        pr(i),...
        T2_pr,T1_pr(i),rho2_pr,rho1_pr(i),r2,r1,Rgas,M2,M1,k12);
    % Calculates surface tension of binary mixture
    surf_ten(i) = surface_ten(phi1,phi1_v,T(i),P_eq(i),P1_pr(i),P2_pr,...
        T1_pr(i),T2_pr,rho1_pr(i),rho2_pr,v1_pr,v2_pr,eps11(i),eps22,...
        r1,r2,M1,M2,k12,k11_rd,k22_rd,mi1_eq(i),mi2_eq(i),P_eq(i)); % [mN/m
            ]
    disp('surface_tension = ');disp(surf_ten(i));
end
figure(1)
plot(P_eq,surf_ten,'-k')
xlabel('Pressure(MPa)')
ylabel('surface tension(mN/m)')
```

```
axis([0 210 0 80]);
```

```
function [mi ] = chem_pot_bin( R,phi_root,r1,r2,phi2,r1_0,rho_bin_par,rho_
    bin,P1_pr,P2_pr,Pmatr,T1_rd,T,P1_rd )
%this function calculates the chemical potential of the binary mixture

mi = R*T.*(log(phi_root) + (1-r1/r2).*phi2 + r1_0*rho_bin_par.*...
    ((P1_pr+P2_pr-2*Pmatr(1,2))./(P1_pr.*T1_rd)).*phi2.^2) + ...
      r1_0*R*T.*(-rho_bin_par./T1_rd + P1_rd./(rho_bin.*T1_rd) ...
      + (1./rho_bin).*(( 1 - rho_bin_par).*log(1-rho_bin_par) + ...
      (rho_bin_par/r1_0).*log(rho_bin_par)));
end
```

```
function  mi= chem_potnew(T,rho_rd,P_rd,T_rd,r)

R=8.3144621; % gas constant
mi=r*R*T*(-(rho_rd/T_rd) + (P_rd/(rho_rd*T_rd)) +(1-rho_rd)*log(1-rho_rd)/
    rho_rd + (1/r)*log(rho_rd));
```

```
function h = eos24cnew(rho_rd,T_rd,P_rd,r)
% EOS (24c), Sanchez and Lacombe (1976)

h = 1 - exp(-rho_rd.^2./T_rd - (1-1./r).*rho_rd - P_rd./T_rd);
```

```
function [rad] = EOS1_anew(P_rd_root, T_rd_root,r_root)
% this function calculates the liquid density, representing the root of EOS
% equation with the maximum value
% Reference
    ************************************************************************

% Sanchez & Lacombe (1976). An Elementary Molecular Theory of Classical
    Fluids
% J. Chem. Phys. Vol. 80, N.21, 2352-2362.
%
    ************************************************************************


rho_rd_root = linspace(-0.1,0.99999,100);
IRoots = sign(eosrootsnew(rho_rd_root,T_rd_root,P_rd_root,r_root));
K=0;
for i=2:length(IRoots)
    flag(i) = IRoots(i) + IRoots(i-1);
    if flag (i) == 0
        K=K+1;
        X0(K,1) = rho_rd_root(i-1);
        X0(K,2) = rho_rd_root(i);
    end;
end;
for k=1:K
                                                                    %
    find roots
    rad(k) = fzero(@(rho_rd_root) eosrootsnew(rho_rd_root,T_rd_root,P_rd_
        root,r_root), X0(k,:));
end
end
```

```
function [rad] = EOS1_anewbin(P_rd, T_rd,r)

% Reference
    ********************************************************************************

% Sanchez & Lacombe (1976). An Elementary Molecular Theory of Classical
    Fluids
% J. Chem. Phys. Vol. 80, N.21, 2352-2362.
%
    ********************************************************************************


rho_cryt2=5;
rho_cryt1=-1;
r_aux=1-1/r;
discr=4+(T_rd*r_aux)^2 -4*T_rd*r_aux-8*T_rd/r;
if discr>0
    rho_cryt2=-0.25*(T_rd*r_aux -2 -sqrt(discr));
    rho_cryt1=-0.25*(T_rd*r_aux -2 +sqrt(discr));
end
F_cryt1=-rho_cryt1 + 1 - exp(-rho_cryt1.^2./T_rd - (1-1./r).*rho_cryt1 - P_
    rd./T_rd);
F_cryt2=-rho_cryt2 + 1 - exp(-rho_cryt2.^2./T_rd - (1-1./r).*rho_cryt2 - P_
    rd./T_rd);
if rho_cryt1>0 && rho_cryt2<5 && (F_cryt2*F_cryt1)<0
    if 0>=F_cryt1>=-0.1 && (F_cryt2*F_cryt1)<0
        rho_aux = linspace(0,5,100);
        F_aux=-rho_aux + 1 - exp(-rho_aux.^2./T_rd - (1-1./r).*rho_aux - P_
            rd./T_rd);
        IRoots = sign(F_aux);
        K=0;
        for i=2:length(IRoots)
            flag(i) = IRoots(i) + IRoots(i-1);
            if flag (i) == 0
                K=K+1;
                X0(K,1) = rho_aux(i-1);
                X0(K,2) = rho_aux(i);
            end
        end
        for k=1:K
            rad(k)= fzero(@(rho_rd) eosrootsnew(rho_rd,T_rd,P_rd,r), X0(k
                ,:));
        end
        rad=max(rad);
    else
        rad=10;
        disp('too much roots! rad=10');
        pause
    end
else
    rad= fzero(@(rho_rd) eosrootsnew(rho_rd,T_rd,P_rd,r), [0,5]);
end
```

```
function h1 = eosrootsnew(rho_rd,T_rd,P_rd,r)
```

```
h1 = rho_rd - eos24cnew(rho_rd,T_rd,P_rd,r);
```

```
function h=equilibrium_bin(phi_root,T,P,P1_pr,P2_pr,T1_pr,T2_pr,rho1_pr,rho
    2_pr,T1_rd,P1_rd,r1_0,r2_0,R,M1,M2,k12)

rho1 = EOS1_anew(P1_rd, T1_rd,r1_0);
mi1 = chem_potnew(T,rho1,P1_rd,T1_rd,r1_0); % chemical potential of 1 in
    the gas phase, it is equivalent to the pure
                                            % chem. pot. because only
                                                component 1 is present in
                                                the gas phase
for k=1:length(phi_root)
    phi2(k)=1-phi_root(k);
    [rho_bin_rd(k),rho_bin_pr(k),Pmatr]=mix_rules(P,T,phi_root(k),P1_pr,P2_
        pr,T1_pr,T2_pr, rho1_pr,rho2_pr,r1_0,r2_0,M1,M2,k12);
end
rho_bin_par= rho_bin_rd; %.*phi_root;
mi1_binmix = chem_pot_bin(R,phi_root,r1_0,r2_0,phi2,r1_0,rho_bin_par,rho_
    bin_rd,P1_pr,P2_pr,Pmatr,T1_rd,T,P1_rd);
h = mi1_binmix-mi1;
```

```
function [mu] = equilibrium_mu(phiA,T,P,PA_rd,TA_rd,PA_pr,PB_pr,TA_pr,TB_pr
    ,rhoA_pr,rhoB_pr,rA_0,rB_0,R,MA,MB,kAB)

for k=1:length(phiA)
    phiB(k)=1-phiA(k);

    [rho_bin_rd(k),Not2,Pmatr]=mix_rules(P,T,phiA(k),PA_pr,PB_pr,TA_pr,TB_
        pr, rhoA_pr,rhoB_pr,rA_0,rB_0,MA,MB,kAB);
end
rho_bin_par= rho_bin_rd;
mu = chem_pot_bin(R,phiA,rA_0,rB_0,phiB,rA_0,rho_bin_par,rho_bin_rd,PA_pr,
    PB_pr,Pmatr,TA_rd,T,PA_rd);
end
```

```
function [ int ] = integfun( X2,P1_pr,P2_pr,T1_pr,T2_pr,rho1_pr,rho2_pr,v1_
    pr,v2_pr,r1,r2,M1,M2,k12,...
    mi1_eq,mi2_eq,P_eq,T  )
% Integrand function
R=8.3144621;
T1_rd=T./T1_pr;
P1_rd=P_eq/P1_pr;
X=1-X2;
rho_bin_rd=zeros(1,length(X));
Not2=zeros(1,length(X));
vbin_pr_l=zeros(1,length(X));
phi2=zeros(1,length(X));
for i=1:length(X)
    [rho_bin_rd(i),Not2(i),Pmatr]=mix_rules(P_eq,T,X(i),P1_pr,P2_pr,T1_pr,T
        2_pr, rho1_pr,rho2_pr,r1,r2,M1,M2,k12);
    vbin_pr_l(i)=X(i)*v1_pr + (1-X(i))*v2_pr;  % [cm^3/mol] Lacombe and
        Sanchez, 1976, eq.19
    phi2(i)=1-X(i);
    rho_bin_par(i)= rho_bin_rd(i);
end
```

```
mu = chem_pot_bin(R,X,r1,r2,phi2,r1,rho_bin_par,rho_bin_rd,P1_pr,P2_pr,
    Pmatr,T1_rd,T,P1_rd);
par_den1= rho_bin_rd.*vbin_pr_l;
Delta_A=abs(par_den1.*(mu -mi1_eq));
int = rho_bin_rd.*sqrt(Delta_A).*(1./vbin_pr_l); % [(mol/cm^3)((J/cm^3)
    ^1/2)]
end
```

```
function [ int ] = integral( P1_pr,P2_pr,T1_pr,T2_pr,rho1_pr,rho2_pr,v1_pr,
    v2_pr,r1,r2,M1,M2,k12,PHI2_II,...
    PHI2_I,mi1_eq,mi2_eq,P_eq,T )
% Integral eq. 8 Harrison et al., 1996

R=8.3144621;
phi_plot=linspace(0,0.999,1000);
T1_rd=T./T1_pr;
P1_rd=P_eq/P1_pr;
phi2=zeros(1,length(phi_plot));
rho_bin_rd=zeros(1,length(phi_plot));
Not2=zeros(1,length(phi_plot));
vbin_pr_l=zeros(1,length(phi_plot));
for k =1:length(phi_plot)
    phi2(k)=1-phi_plot(k);
    [rho_bin_rd(k),Not2(k),Pmatr]=mix_rules(P_eq,T,phi_plot(k),P1_pr,P2_pr
        ,...
                                T1_pr,T2_pr, rho1_pr,rho2_pr,r1,r2,M1,M2,
                                    k12);
    vbin_pr_l(k)=phi_plot(k)*v1_pr + phi2(k)*v2_pr;
end
rho_bin_par= rho_bin_rd;
phi_aux=1-PHI2_II;
[rho_aux,rho_bin_pr,Not3] = mix_rules(P_eq,T,phi_aux,P1_pr,P2_pr,T1_pr,T2_
    pr, rho1_pr,rho2_pr,r1,r2,M1,M2,k12);
rho1_rd = EOS1_anew(P1_rd, T1_rd,r1);
% ------------------------linear density profile---------------------------
mu = chem_pot_bin(R,phi_plot,r1,r2,phi2,r1,rho_bin_par,rho_bin_rd,P1_pr,P2_
    pr,Pmatr,T1_rd,T,P1_rd);
% plot Free Energy profile
par_den1= rho_bin_rd.*vbin_pr_l;
Delta_A_plot=par_den1.*(mu -mi1_eq);
D=par_den1.*mu;
H=par_den1.*mi1_eq;
figure(3)
plot(phi_plot,H);
xlabel('water volume fraction')
ylabel('Free Energy (J/mol)');
hold on
figure(3)
plot(phi_plot,D,'r');
hold on
pause
close all
int = quad(@(X) integfun(X,P1_pr,P2_pr,T1_pr,T2_pr,rho1_pr,rho2_pr,v1_pr,v
    2_pr,r1,r2,M1,M2,k12,...
    mi1_eq,mi2_eq,P_eq,T),PHI2_I,PHI2_II); %[(1/cm^3)((J/cm^3)^1/2)]
end
```

```
function [rho_rd,rhobin_pr,Pmatr] = mix_rules(P,T,phiA,P1_pr,P2_pr,T1_pr,T
    2_pr, rho1_pr,rho2_pr,r1,r2,M1,M2,k12)
% Mixing rules for binary mixture (Lacombe Sanchez, 1976, Sato et al.,
    1996)

            Rgas=8.3144621;          % gas constant (J/mol*K)
            P12=(1-k12)*sqrt(P1_pr*P2_pr); % eq.8 (Sato et al., 1996);
                modified from eq.79 (Lacombe Sanchez, 1976)
            P21=P12; %sqrt(P1_pr*P2_pr);
            P11=P1_pr;
            P22=P2_pr;
            Pmatr=[P11,P12;P21,P22];
            P2_rd = P./P2_pr;
            T2_rd= T./T2_pr;
            phiB=1-phiA;
            phi=[phiA,phiB]; % phi vector eq. 12
            Pbin_pr= ((phiA*phiA*P11)+(phiA*phiB*P12))  + ((phiB*phiA*P21)
                +(phiB*phiB*P22));%phiA*phiB*P12; %dot(phi,(phi*Pmatr));  %
                 eq.7
            Pbin_rd=P./Pbin_pr;
            phiA_0=(phiA.*P1_pr./T1_pr)./((phiA.*P1_pr./T1_pr)+(phiB.*P2_pr
                ./T2_pr));
            phiB_0=(phiB.*P2_pr./T2_pr)./((phiA.*P1_pr./T1_pr)+(phiB.*P2_pr
                ./T2_pr));
            phi_0=[phiA_0,phiB_0];   % phi_0 vector eq.11
            Tbin_pr=Pbin_pr*(phiA_0*T1_pr/P1_pr + phiB_0*T2_pr/P2_pr); %sum
                (phi_0*Tcd_pr./Pcd_pr); % eq.9
            Tbin_rd=T./Tbin_pr;
            r1_0 = r1;
            r2_0 = r2;
            A=(phiA_0/r1_0)+(phiB_0/r2_0);%(phiA_0/r1_mod)+(phiB_0/r2_mod);
            rbin=1./A;
            w1= (phiA.*rho1_pr)./(rho2_pr-(phiA.*rho2_pr) + (phiA.*rho1_pr)
                ); % weight fraction
            w2= (phiB.*rho2_pr)./(rho1_pr-(phiB.*rho1_pr) + (phiB.*rho2_pr)
                );
            v1=Rgas*T1_pr/P1_pr;
            v2=Rgas*T2_pr/P2_pr;
            v1_aux=v1*rho1_pr;
            v2_aux=v2*rho2_pr;
            x1=(w1/v1_aux)/(w1/v1_aux + w2/v2_aux);  % molar fraction
            x2=(w2/v2_aux)/(w1/v1_aux + w2/v2_aux);
            rhobin_pr=1e6*(M2*x2+M1*x1)*Pbin_pr/(Rgas*Tbin_pr*rbin);% eq.
                10
            rho_rd = EOS1_anewbin(Pbin_rd, Tbin_rd,rbin);
end
```

```
function  DeltaA  = plot_aux( X,P1_pr,P2_pr,T1_pr,T2_pr,rho1_pr,rho2_pr,v1_
    pr,v2_pr,r1,r2,M1,M2,k12,...
    mi1_eq,mi2_eq,P_eq,T  )

for i=1:length(X)
    [rho_rd_l(i),Tbin_rd_l(i),rbin(i),Pbin_pr(i)] = mix_rules_integ(P_eq,T,
        X(i),P1_pr,P2_pr,T1_pr,T2_pr, rho1_pr,rho2_pr,r1,r2,M1,M2,k12);
```

```
    vbin_pr_l(i)=X(i)*v1_pr + (1-X(i))*v2_pr;  % [cm^3/mol] Lacombe and
        Sanchez, 1976, eq.19
end
DeltaA = plot_G(X,Pbin_pr,vbin_pr_l,rbin,r1,r2,rho_rd_l,...
    Tbin_rd_l,mi1_eq,mi2_eq,P_eq);         % [J/cm^3]
end
```

```
function [ DeltaA ] = plot_G(X,Pbin_pr,vbin_pr_l,rbin,r1,r2,rho_rd_l,...
    Tbin_rd_l,mi1_eq,mi2_eq,P_eq)

X2 = 1-X; % mer fraction [adim]
v_rd_l = 1./rho_rd_l;
DeltaA = (Pbin_pr.*rho_rd_l).*(-rho_rd_l + Tbin_rd_l.*...
    ((v_rd_l-1).*log(1-rho_rd_l) + (1./rbin).*log(rho_rd_l) + ...
    (X./r1).*log(X) + (X2./r2).*log(X2))) + P_eq - (rho_rd_l./(vbin_pr_l))
        .*...
    (X.*mi1_eq + X2.*mi2_eq);  % [J/cm^3=MPa] eq.54 Poser and Sanchez, 1981
G1=(Pbin_pr.*rho_rd_l).*(-rho_rd_l + Tbin_rd_l.*...
    ((v_rd_l-1).*log(1-rho_rd_l) + (1./rbin).*log(rho_rd_l) + ...
    (X./r1).*log(X) + (X2./r2).*log(X2)))+P_eq;
G2=(rho_rd_l./(vbin_pr_l)).*...
    (X.*mi1_eq + X2.*mi2_eq);
figure(5)
plot(X,G1,'r')
hold on
figure(5)
plot(X,G2)
hold on
figure(6)
plot(X,rho_rd_l);
hold on
end
```

```
function [rad] = root_bin( R,T,P,r1,r2,P1_pr,P2_pr,T1_pr,T2_pr,rho1_pr,rho
    2_pr,M1,M2,k12)

P1_rd=P./P1_pr;
T1_rd=T./T1_pr;
phi_root = linspace(0.00001,0.2,100);
IRoots = sign(equilibrium_bin(phi_root,T,P,P1_pr,P2_pr,T1_pr,T2_pr,rho1_pr,
    rho2_pr,T1_rd,P1_rd,r1,r2,R,M1,M2,k12));
K=0;
for i=2:length(IRoots)                                  % find intervals
    where function changes sign
    flag(i) = IRoots(i) + IRoots(i-1);
    if flag (i) == 0
        K=K+1;
        X0(K,1) = phi_root(i-1);
        X0(K,2) = phi_root(i);
    end
end
if K==0
    rad=2;
else
    for k=1:K       % find roots
```

```
        rad_temp(k) = fzero(@(phi_root) equilibrium_bin(phi_root,T,P,P1_pr,
            P2_pr,T1_pr,T2_pr,rho1_pr,rho2_pr,T1_rd,P1_rd,r1,r2,R,M1,M2,k
            12), X0(k,:));

        if K>1
            phiA= rad_temp(k);
            [rho_test_rd,rho_bin_pr,Not3] = mix_rules(P,T,phiA,P1_pr,P2_pr,
                T1_pr,T2_pr, rho1_pr,rho2_pr,r1,r2,M1,M2,k12);
            rho_test(k) = rho_test_rd*rho_bin_pr;
        end
    end
    rad=rad_temp(1);
    if K>1
        [rho_test_min,ind] = min(rho_test(1:K));
        rad=rad_temp(ind);
        disp('K>1');
    end
end
```

```
function phi1 = solubility( k12,T,P, P2_pr, P1_pr, T1_pr,T2_pr,rho1_pr,rho
    2_pr,R,r1,r2,M1,M2)

% 1=water
for i=1:length(P)
    phi1(i)= root_bin(R,T(i),P(i),r1,r2,P1_pr,P2_pr,T1_pr,T2_pr,rho1_pr,rho
        2_pr,M1,M2,k12);
end
end
```

```
function [ sigma ] = surface_ten(phi1_l,phi1_v,T,P,P1_pr,P2_pr,T1_pr,T2_pr
    ,...
    rho1_pr,rho2_pr,v1_pr,v2_pr,eps11,eps22,r1,r2,M1,M2,...
    k12,k11_tilde,k22_tilde,mi1_eq,mi2_eq,P_eq )
% Surface Tension of a binary mixture

Rgas=8.3144621;        % Gas constant [J/(mol*K)]
NA = 6.022136736*1e23; % Avogadro Number [1/mol]
% liquid phase
[rho_rd_l,rhobin_pr,Pmatr] = mix_rules(P,T,phi1_l,P1_pr,P2_pr,T1_pr,T2_pr,
    rho1_pr,rho2_pr,r1,r2,M1,M2,k12);
vbin_pr_l=phi1_l*v1_pr + (1-phi1_l)*v2_pr;  % [cm^3/mol] Lacombe and
    Sanchez, 1976, eq.19
% vapour phase
P1_rd=P./P1_pr;
T1_rd=T./T1_pr;
rho_rd_v = EOS1_anew(P1_rd, T1_rd,r1);
vbin_pr_v=v1_pr;   % [cm^3/mol]
% Densities
phi2_l = 1-phi1_l; % mer fraction [adim]
phi2_v = 0;
rho1_l = phi1_l.*rho_rd_l./vbin_pr_l; % [mol/cm^3], Poser and Sanchez,
    1981, eq.53
rho2_l = phi2_l.*rho_rd_l./vbin_pr_l;
rho1_v = phi1_v.*rho_rd_v./vbin_pr_v;
rho2_v = phi2_v.*rho_rd_v./vbin_pr_v;
```

```
Delta_rho1 = rho1_l - rho1_v; % [mol/cm^3]
Delta_rho2 = rho2_l - rho2_v;
PHI2_II = phi2_l; % [adim]
PHI2_I = phi2_v;
% surface tension
k11 = 2*P1_pr*((v1_pr)^(8/3))*k11_tilde;  % eq. 15 (Harrison et al., 1996)
    [cm^5 J/mol]
k22 = 2*P2_pr*((v2_pr)^(8/3))*k22_tilde;
integ = integral(P1_pr,P2_pr,T1_pr,T2_pr,rho1_pr,rho2_pr,v1_pr,v2_pr,r1,r2,
    M1,M2,k12,PHI2_II,...
                              PHI2_I,mi1_eq,mi2_eq,P_eq,T );
sigma = sqrt(2)*abs(sqrt(k22) + sqrt(k11).*(Delta_rho1./Delta_rho2)).*integ
    ; % Equation from Harrison et al., 1996
sigma = sigma*1e-3; % [mN/m]
```

BIBLIOGRAPHY

N.K. Adams, B.F. Houghton, and W. Hildreth. Abrupt transitions during sustained explosive eruptions: examples from the 1912 eruption of novarupta, alaska. *Bulletin of Volcanology*, 69:189–206, 2006.

A. Austin Erickson, R. BÃijttner, P. Dellino, M.H. Ort, and B. Zimanowski. Phreatomagmatic explosions of rhiolitic magma: experimental and field evidence. *Journal of Geophysical Research*, 113:B11201, 2009.

N.S. Bagdassarov and D.B. Dingwell. Deformation of foamed rhyolite under internal and external stresses: an experimental investigation. *Bulletin of Volcanology*, 55:147–154, 1993.

N.S. Bagdassarov, N.A. Dorfman, and D.B. Dingwell. Effect of alkalis, phosphorus, and water on the surface tension of haplogranite melt. *American Mineralogist*, 85:33 âĂŞ 40, 2000.

F. Barberi, F. Innocenti, L. Lirer, R. Munno, T.S. Pescatore, and R. Santacroce. The campanian ignimbrite: a major prehistoric eruption in the neapolitan area (italy). *Bulletin of Volcanology*, 41:10–22, 1978.

J.D. Blower, J.P. Keating, H.M. Mader, and J.C. Phillips. The evolution of bubble size distributions in volcanic eruptions. *Journal of Volcanology and Geothermal Research*, 20:1–23, 2002.

R. Buttner and B. Zimanowky. Physics of thermohydraulic explosions. *American Physical Society*, 57, 5:5726–5729, 1997.

R. Buttner, P. Dellino, and B. Zimanowsky. Identifying modes of magma/water interaction from the surface features of ash particles. *Nature*, 401:688–690, 1999.

R. Buttner, P. Dellino, L. La Volpe, V. Lorenz, and B. Zimanowsky. Thermohydraulic explosions in phreatomagmatic eruptions as evidenced by the comparison between pyroclasts and products from molten fuel coolant interaction experiments. *Journal of Geophysical Research*, 107(B11):2277, 2002.

R. Buttner, P. Dellino, H. Raue, I. Sonder, and B. Zimanowsky. Stress-induced brittle fragmentation of magmatic melts: theory and experiments. *Journal of Geophysical Research*, 111:1–10, 2006.

J.W. Cahn and J.E. Hilliard. Free energy of a nonuniform system. i. interfacial free energy. *Journal of Chemical Physics*, 28:258âĂŞ267, 1959.

R.J. Carey, B.F. Houghton, and T. Thordarson. Abrupt shifts between wet and dry phases of the 1875 eruption of askja volcano: microscopic evidence for microscopic conduit dynamics. *Journal of Volcanology and Geothermal Research*, 184:256–270, 2009.

K.V. Cashman and M.T. Mangan. Physical aspects of magmatic degassing. ii. constraints on vesiculation processes from textural studies of eruptive products. *Carroll MR, Holloway JR (eds) Volatiles in Magmas. Review in Mineralalogy*, 30:447âĂŞ478, 1994.

L. Civetta, G. Orsi, L. Pappalardo, R.V. Fisher, G. Heiken, and M. Ort. Geochemical zoning, mingling, eruptive dynamics and depositional processes - the campanian ignimbrite, campi flegrei, italy. *Journal of Volcanoloy and Geothermal Research*, 75:183–219, 1997.

G. De Natale. The campi flegrei caldera: Unrest mechanisms and hazards. *in Mechanisms of Activity and Unrest at Large Calderas, edited by C. Troise, G. De Natale, and C. Kilburn, Geological Society of London, London*, 269:25 âĂŞ 45, 2006.

D. De Rita, D. Dolfi, C. Tersigni, and R. Trigila. Alcuni risultati sperimentali sulla solubilitÃă dell'h$_2$o nella 'ignimbrite campana' a p_{H_2O} fra 10.000 e 30.000 p.s.i. *Periodico di Mineralogia e Petrologia*, 73:47âĂŞ65, 1976.

B. De Vivo, G. Rolandi, P.B. Gans, A. Calvert, W.A. Bohrson, F.J. Spera, and H. Belkin. New constraints on the pyroclastic eruptive history of the campanian volcanic plain (italy). *Rendiconti della SocietÃă Italiana di Mineralogia e Petrologia*, 33(1):73–80, 1976.

P. Dellino and L. La Volpe. Image processing analysis in reconstructing fragmentation and transportation mechanisms of pyroclastic deposits. the case of monte pilato-rocche rosse eruptions, lipari (aeolian islands, italy). *Journal of Volcanology and Geothermal Research*, 71:13âĂŞ29, 1996a.

P. Dellino and L. La Volpe. Cluster analysis on ash particles morphology features to discriminate fragmentation dynamics in explosive eruptions. *Acta Vulcanologica*, 1:31–39, 1996b.

P. Dellino, R. Isaia, L. La Volpe, and G. Orsi. Statistical analysis of textural data from complex pyroclastic sequences: implications for fragmentation processes of the agnano-monte spina tephra (4.1 ka), phlegraean fields, southern italy. *Bulletin of Volcanology*, 63:443–461, 2001.

V. Di Matteo, M.R. Carroll, H. Behrens, F. Vetere, and R.A. Brooker. Water solubility in trachytic melts. *Chemical Geology*, 213:187–196, 2004.

S. Enders, H. Kahl, and J. Winkelmann. Interfacial properties of polystyrene in contact with carbon dioxide. *Fluid Phase Equilibria*, 228âĂŞ229:511âĂŞ522, 2005.

M.B. Epelbaum, I. V. Babashov, and T. P. Salova. Temperatures and pressures. *Geochemical International Journal*, 10(12):343 âĂŞ 345, 1973.

R.V. Fisher, G. Orsi, M. Ort, and G. Heiken. Mobility of a large-volume pyroclastic flow-emplacement of the campanian ignimbrite, italy. *Journal of Volcanology and Geothermal Research*, 56:205–220, 1993.

S.J. Fowler, F. J. Spera, W. A. Bohrson, H. E. Delkin, and B. De Vivo. Phase equilibria constraints on the chemical and physical evolution of the campanian ignimbrite. *Journal of Petrology*, 48:459âĂŞ493, 2007.

C. Freda, D. R. Baker, C. Romano, and P. Scarlato. Water diffusion in natural potassic melts. *Geological Society, London, Special Publications*, 213:53 âĂŞ 62, 2003.

H. Gaonac'h, H.J. Stix, and S. Lovejoy. Scaling effects on vesicle shape, size and heterogeneity of lavas from mount etna.scaling effects on vesicle shape, size and heterogeneity of lavas from mount etna. *Journal of Volcanology and Geothermal Research*, 74 (1âĂŞ2):131âĂŞ153, 1996.

J.E. Gardner. Surface tension and bubble nucleation in phonolite magmas. *Geochimica et Cosmochimica Acta*, 76:93–102, 2012.

J.E. Gardner and R.A. Ketcham. Bubble nucleation in rhyolite and dacite melts: Temperature dependence of surface tension. *Contributions to Mineralogy and Petrology*, 162:929–943, 2011.

J.E. Gardner, M. Hilton, and M.R. Carroll. Experimental constraints on degassing of magma: isothermal bubble growth during continuous decompression from high pressure. *Earth and Planetary Science Letters*, 168:201–218, 1999.

M.S. Ghiorso and R.O. Sack. Chemical mass transfer in magmatic processes: Iv. a revised and internally consistent thermodynamic model for the interpolation and extrapolation of liquid-solid equilibria in mag- matic systems at elevated temperatures and pressures. *Contributions to Mineralogy and Petrology*, 119: 197âĂŞ212, 1995.

K.L. Harrison, K.P. Johnston, and I.C. Sanchez. Effect of surfactants on the interfacial tension between supercritical carbon dioxide and polyethylene glycol. *Langmuir*, 12:2637–2644, 1999.

G. Heiken and H.K. Wohletz. *Volcanic ash*. Univerity of California Press, 1985.

S. Hurwitz and O. Navon. Bubble nucleation in rhyolitic melts: experiments at high pressure temperature and water content. *Earth and Planetary Science Letters*, 122:267–280, 1994.

H. Kahl and S. Enders. Calculation of surface properties of pure fluids using density gradient theory and saft-eos. *Fluid Phase Equilibria*, 172:27–42, 2000.

N.I. Khitarov, Y.B. Lebedev, A.M. Dorfman, and N.S. Bagdasarov. Effect of temperature, pressure and volatiles on the surface tension of molten basalt. *Geochemical International Journal*, 16:78–86, 1979.

L.D. Landau and E.M. Lifshitz. *Course of Theoretical Physics Vol.5, Statistical Physics*. Rober Maxwell, M.C., 1980.

R.L. Lange and I.S.E. Carmichael. Thermodynamic properties of silicate liquids with emphasis on density, thermal expansion and compressibility. *Mineralogical Society of America, Review in Mineralogy*, 24:25–64, 1990.

H. Machida, Y. Sato, and Jr.R.L. Smith. Simple modification of the temperature dependence of the sanchez-lacombe equation of state. *Fluid Phase Equilibria*, 297:205–209, 2010.

M.T. Mangan and K.V. Cashman. The structure of basaltic scoria and reticulite and inferences for vesiculation, foam formation, and fragmentation in lava fountains. *Journal of Volcanoloy and Geothermal Research*, 73:1–18, 1996.

M.T. Mangan and T. Sisson. Delayed, disequilibrium degassing in rhyolite magma: Decompression experiments and implications for explo- sive volcanism. *Earth and Planetary Science Letters*, 183:441âĂŞ455, 2000.

M.T. Mangan and T. Sisson. Evolution of melt-vapor surface tension in silicic volcanic systems: Experiments with hydrous melts. *Journal of Geophysical Research*, 110:1âĂŞ9, 2005.

M.T. Mangan, K.V. Cashman, and S. Newman. Vesiculation of basaltic magma during eruption. *Geology*, 21:157âĂŞ160, 1993.

G. Mastrolorenzo, L. Brachi, and A. Canzanella. Vesicularity of various types of pyroclastic deposits of campi flegrei volcanic field: evidence of analogies in magma rise and vesiculation mechanisms. *Journal of Volcanology and Geothermal Research*, 109:41âĂŞ53, 2001.

C.C. Mourtada Bonnefoi and D. Laporte. Experimental study of homogeneous bubble nucleation in rhyolitic magmas. *Geophysical Research Letters*, 26:3505–3508, 1999.

O. Navon and V. Lyakhovsky. Vesiculation processes in silicic magmas. *Geological Society, London, Special Publications*, 145:27–50, 1998.

D.M. Palladino and E. Agosta. Pumice fall deposits of the western vulsini volcanoes (central italy). *Journal of Volcanology and Geothermal Research*, 78: 77–102, 1997.

D.M. Palladino and J. Taddeucci. The basal ash deposit of the sovana eruption (vulsini volcanoes, central italy): the product of a dilute pyroclastic density current. *Journal of Volcanology and Geothermal Research*, 87:233–254, 1998.

D.M. Palladino and G.A. Valentine. Coarse-tail vertical and lateral grading in pyroclastic flow deposits of the latera volcanic complex (vulsini, central italy): origin and implications for flow dynamics. *Journal of Volcanology and Geohermal Research*, 69:343–364, 1995.

D.M. Palladino, S. Simei, and S. Kyriakopoulos. On magma fragmentation by conduit shear stress: evidence from the kos plateau tuff, aegean volcanic arc. *Journal of Volcanology and Geothermal Research*, 178:807–817, 2008a.

D.M. Palladino, S. Simei, and R. Trigila. The campanian active volcanoes: Somma-vesuvius and campi flegrei. *Guide book, 70th EAGE Conference*, pages 1–33, 2008b.

D.M. Palladino, G. Sottili, S. Simei, and R. Trigila. Integrated approach for the reconstruction of stratigraphy and geology of quaternary volcanic terrains: an application to the vulsini volcanoes (central italy). *In G. Groppelli e L. Viereck (Eds.), "Stratigraphy and geology in volcanic areas", Geological Society of America, Special Paper*, 464:66–84, 2010.

M. Polacci, P. Papale, and M. Rosi. Textural heterogeneities in pumices from the climactic eruptions of mount pinatubo, 15 june 1991, and implications for magma ascent dynamics. *Bulletin of Volcanology*, 63:83âĂŞ97, 2001.

M. Polacci, L. Pioli, and M. Rosi. The plinian phase of the campanian ignimbrite eruption (phlegrean fields, italy): evidence from density measurements and textural characterization of pumice. *Bulletin of Volcanology*, 65:418âĂŞ432, 2003.

M. Polacci, D.R. Baker, L. Mancini G. Tromba, and F. Zanini. Three-dimensional investigation of volcanic textures by x-ray microtomography and implications for conduit processes. *Geophysical Research Letters*, 33:L13312, 2006.

M. Polacci, L. Mancini, and D.R. Baker. The contribution of synchrotron x-ray computed microtomography to understanding volcanic processes. *Journal of Synchrotron Radiation*, 17:215–221, 2010.

C.I. Poser and I.C. Sanchez. Surface tension theory of pure liquids and polymer melts. *Journal of Colloid and Interface Science*, 69-3:539âĂŞ548, 1979.

C.I. Poser and I.C. Sanchez. Interfacial tension theory of low and high molecular weight liquid mixtures. *Macromolecules*, 14:361âĂŞ370, 1981.

A.A. Proussevitch and D.L. Sahagian. Dynamics and energetics of bubble growth in magmas: Analytical formulation and numerical modelling. *Journal of Geophysical Research*, 103:18,223âĂŞ18,251, 1998.

A.A. Proussevitch, D.L. Sahagian, and A.T. Anderson. Dynamics of diffusive bubble growth in magmas: isothermal case. *Geophysical Research Letters*, 98(B12): 22283–22307, 1993.

A.A. Proussevitch, D.L. Sahagian, and P.E. Tsentalovich. Statistical analysis of bubble and crystal size distributions: Formulations and procedures. *Journal of Volcanology and Geothermal Research*, 164, 3:95âĂŞ111, 2007.

A.A. Proussevitch, G.K. Mulukutla, and D.L. Sahagian. A new 3d method of measuring bubble size distributions from vesicle fragments preserved on surfaces of volcanic ash particles. *Geosphere*, 7, 1:1âĂŞ8, 2011.

M. Rosi, L. Vezzoli, P. Aleotti, and M. De Censi. Interaction between caldera collapse and eruptive dynamics during the campanian ignimbrite eruption, phlegraean fields, italy. *Bulletin of Volcanology*, 57:541–554, 1996.

A.C. Rust and M. Manga. Bubble shapes and orientations in low re simple shear flow. *Journal of Colloid and Interface Science*, 249:476–480, 2002.

D.L. Sahagian and A.A. Proussevitch. 3d particle size distributions from 2d observations: stereology for natural applications. *Journal of Volcanology and Geothermal Research*, 84:173âĂŞ196, 1998.

I.C. Sanchez and R.H. Lacombe. An elementary molecular theory of classical fluids: Pure fluids. *Journal of Chemical Physics*, 80:2352, 1976.

R.S.J. Sparks. Stratigraphy and geology of the ignimbrites of vulsini volcano, italy. *Geologische Rundschau*, 64:497–523, 1975.

J. Taddeucci and D.M. Palladino. Particle size-density relationships in pyroclastic deposits: inferences for emplacement processes. *Bulletin of Volcanology*, 64: 273–284, 2002.

A. Toramaru. Vesciculation process and bubble size distributions in ascending magmas with constant velocities. *Journal of Geophysical Research*, 94:17523–17542, 1989.

A. Toramaru. Measurement of bubble size distribution in vesiculated rocks with implications for quantitative estimation of eruption process. *Journal of Volcanology and Geothermal Research*, 43:71–90, 1990a.

A. Toramaru. Numerical study of nucleation and growth of bubbles in viscous magmas. *Journal of Geophysical Research*, 100:1913–1931, 1990b.

A. Toramaru. Bnd (bubble number density) decompression rate meter for explosive volcanic eruptions. *Journal of Volcanology and Geothermal Research*, 154:303–316, 2006.

R. Trigila, M. Battaglia, G. Sottili, and M. Brilli. Volcanic eruptions from ghost magma chambers. *Journal of Geophysical Research*, 35:1–5, 2008.

L. Vezzoli, S. Conticelli, F. Innocenti, P. Landi, P. Manetti, D.M. Palladino, and R. Trigila. Stratigraphy of the latera volcanic complex: proposals for a new nomenclature. *Periodico di Mineralogia*, 56:89–100, 1987.

K.H. Wohletz. Mechanisms of hydrovolcanic pyroclast formation: grain-size, scanning electron microscopy and experimental studies. *Journal of Volcanology and Geothermal Research*, 17:65–88, 1983.

K.H. Wohletz. Explosive magma-water interactions: thermodynamics, explosion mechanism and field studies. *Bulletin of Volcanology*, 48:245–264, 1986.

K.H. Wohletz, G. Orsi, and S. de Vita. Eruptive mechanisms of the neapolitan yellow tuff interpreted from stratigraphic ,chemical and granulometric data. *Journal of Volcanology and Geothermal Research*, 67:263–290, 1995.